In the first place, the authors want to thank the editor and reviewers for the time expended in reviewing our manuscript and writing their reports. We made a thorough revision of the manuscript taking into account all the comments. In what follows we answer each comment in particular. Also a version of the manuscript with the changes highlighted is included at the end of this document.

Comments from Reviewer 1

1. *Abstract, Line 19: Possible typo, should it not be "phase averaging"?*

Response: The authors thank the reviewer for pointing this out. The term has been corrected to 'phase averaging' in the revised manuscript (Abstract, lines 11 and 18).

2. *Line 28, I am not sure that the term "latter" works in this syntax. Please rephrase*

Response: The authors agree with the reviewer's suggestion. The sentence has been rephrased for better clarity (Introduction, line 26).

3. *Line 33, The description of the work of Schulz et al., is not clear, especially in the distinction between quasi-steady and unsteady effects. What are these unsteady effects? I believe that in this work Schulz refers to the returning wake effect. I am thinking that there might be no need to provide a description about unsteady effects in this part of the manuscript, and the authors should consider eliminating this part of the sentence.*

Response: The authors appreciate the reviewer's suggestion. Following this recommendation, the description of unsteady effects regarding the work of Schulz et al. has been removed to avoid confusion (Introduction, line 33).

4. *In the UNAFLOW campaign described in the work by Fontanella et al., 2022, the authors used a uniform inflow with about 2% TI. While the wind tunnel can be used to investigate the impact of ABL on structures and wind turbines, no ABL was considered in this or subsequent studies on the same FOWT model.*

Response: The authors thank the reviewer for this clarification regarding the UNAFLOW campaign. The text has been corrected in the Introduction, line 83.

5. *Line 112, I am not sure that the term "considered" is right when describing the hub height. I would suggest simplifying to "the hub height is [...]"*

Response: The authors thank the reviewer for the suggestion. The phrasing has been corrected in the revised manuscript (Numerical Setup, line 119).

6. *What was the blockage ratio during the experiments?*

Response: The blockage ratio during the experiments was 0.5%. This information has been added to the revised manuscript (Numerical Setup, line 118).

7. *Is it needed to provide the governing equations in the manuscript? If I am not mistaken, the authors did not modify them in comparison to their usual implementation. In that case, I am not sure that it is necessary to report them here.*

Response: Following the reviewer's suggestion, the governing equations have been removed from Section 2.1 (Numerical Model, line 130), as the implementation follows the standard formulations previously established in the literature.

8. *Line 135, typo, "applied in", I think it should be "applied to"*

Response: The authors thank the reviewer. The typo has been corrected to 'applied to' in the revised manuscript (Section 2.1, line 140).

9. *Line 137: how was the perturbation added in the turbulent case? Did the authors match the turbulent spectra from the wind tunnel? As further details about the inflow are provided in the following sections, the authors should highlight for the interested reader where the additional inflow information is provided.*

Response: The authors have clarified this point in the revised manuscript. A filtered noise boundary condition (based on Klein et al., 2003) was used to match the turbulent length scales of the ABL case. As suggested, in line 144, we have explicitly directed the reader to Section 2.3 for a comprehensive description of the inflow generation and the scaling process used to achieve the target flow.

10. *Line 141, how is the method different from the implementation in the literature?*

Response: The AD approach used here differs from the one presented in Navarro Diaz et al. (2019a, b, 2021) in two main aspects: (i) the nodes are organised in a ring-based layout instead of lines, and (ii) a constant thrust coefficient (C_t) is assumed. Given that these are minor implementation adjustments rather than a fundamental change in the underlying physics, the authors believe there is no need for a detailed description in the text.

11. *Eq (5): I am struggling to follow the reasoning of the authors in this part of the manuscript and I believe that clarity could be improved. When inserting the forces in the domain, when a motion of the platform is considered, I would imagine that the forces are proportional to the relative velocity (i.e., to the vector sum of inflow speed and the structural velocity). Why does the structural velocity not appear in Eq. (5)? Since the thrust coefficient is assumed constant (line 159) would the impact of motion not affect the inserted loads through a variation in apparent inflow speed?*

Response: The authors agree with the reviewer's observation. The thrust force is indeed calculated based on the relative velocity. The text in Section 2.2 (lines 160-166) has been revised to explicitly state how the motion of the platform affects the apparent inflow speed and, consequently, the loads applied through the Actuator Disk, even when a constant C_t is assumed.

12. *Line 159: As porous disk I imagine the authors are referring to the Actuator disk model? Was the thrust coefficient measured in the wind tunnel? Rather than "assumed" the thrust coefficient would be rather set to match the experiment, in that case. The authors should*

consider clarifying this. Additionally, was the thrust coefficient under platform motion cases verified under platform motion? Did previous work observe that the thrust coefficient can be assumed constant in the range of apparent speeds considered in this work?

Response: The authors thank the reviewer for pointing out this lack of clarity. Indeed, we are referring to the Actuator Disk (AD) model used to represent the physical porous disk from the experiments. The value of $C_T = 0.65$ was not arbitrarily assumed but was set to match the wind tunnel measurements (Aubrun et al., 2019; Schliffke et al., 2024; Hubert et al., 2025). Regarding the platform motion, while the surge kinematics induce a variation in the apparent inflow velocity of approximately $\pm 25\%$, previous experimental campaigns with this specific porous mesh (Aubrun et al., 2019) have shown that its aerodynamic drag coefficient remains largely independent of the Reynolds number within this velocity range. Therefore, keeping C_T constant is physically representative of the rigid porous disk's behaviour under the modelled surge motion. We have clarified these points in Section 2.2 (lines 168-173) and updated the wording as suggested.

13. *Line 161: Why did the authors select a cross section of 10DX10D? If I am not mistaken this would make the cross section of the numerical domain smaller than the wind tunnel one. At this point of the manuscript it is not clear what the relationship between the numerical and experimental results. The authors should clarify why this test case has been selected and why they are matching it in their simulations. If the objective is to use the same thrust coefficient as the one measured in the experiment, should the numerical domain not match the same blockage of the wind tunnel, as this might affect the thrust coefficient?*

Response: The authors have addressed these concerns by clarifying the scope and the setup of the simulations:

(a) Objective: We have clarified in Section 2 (line 119) that while the study uses the same geometric scales and kinematics as the experimental campaigns, the goal is not a direct quantitative validation. Instead, the experiment provides a physically realistic reference framework to isolate and analyse fundamental wake dynamics.

(b) Blockage Ratio: Regarding the domain size, we have added a clarification in Section 2.3 (line 181). A $10D \times 10D$ cross-section results in a blockage ratio of less than 1%. Since this is well below the 5% threshold where confinement effects typically become significant (Sarlak et al., 2016), the domain is wide enough to avoid artificial acceleration and ensures that the C_T remains representative without needing to replicate the exact wind tunnel dimensions, thus preventing an unnecessary increase in computational time.

14. *Line 175, Why 5D height? Should the cross-section not be 10DX10D as previously described in the same section? Or is this difference due to different numerical setups employed for laminar and turbulent simulations? If so, this should be clarified and justified within the text*

Response: The authors thank the reviewer for pointing out this lack of clarity. The reviewer is correct, the domain height differs between the cases. As clarified in Section 2.3 (lines 197-206), the height for the ABL case was set to $5D$ to accurately model the Atmospheric Surface Layer (ASL). This setup, combined with a top stress boundary condition, prevents the artificial decay of turbulence in the upper domain and ensures a consistent ABL profile. Despite the reduced height, the blockage ratio remains low (1.5%), well below the 5% threshold for confinement effects.

15. *Line 182, Why did the authors use a stress BC for both top and bottom boundaries? To match realistic conditions the stress boundary would be placed on the bottom surface only. Additionally, why did the authors use two different models for top and bottom boundary conditions? This should be clarified for the reader*

Response: The authors have clarified this choice in Section 2.3 (lines 214-218). Two different stress boundary conditions were used to maintain a neutral ASL within the truncated domain:

(a) Bottom boundary: Uses Schumann's model to represent the physical surface roughness of the wind tunnel floor.

(b) Top boundary: Applies a shear-stress condition based on the friction velocity u^*.

This dual configuration provides the necessary forcing to sustain the targeted turbulence levels and prevents the profile from drifting.

16. *Line 190: what does "into consideration" mean in this context? Please clarify*

Response: The authors have rephrased this sentence in Section 2.3 (line 224) to remove the ambiguity. The text now explicitly states that the turbulent length scales used for the filtering process were set equal to the values obtained in the ABL flow.

17. *Sect. 2.4, what is the rotational speed? This value is needed to compute the Strouhal number*

Response: The authors would like to clarify that, since a porous disk model is used to represent a wind turbine in the experimental setup, there is no rotational speed involved. The Strouhal number (St) reported in this work is defined based on the surge frequency (f_{surge}), the disk diameter (D), and the reference velocity (U_{ref}), as specified in Section 1 (line 75) and Table 2.

18. *Section 3,Why did the authors use the term "Preliminary" in the section title? What is preliminar about the outcomes of the studies? Any know limitation of the study should be clearly stated in the manuscript.*

Response: The authors agree that the term 'Preliminary' could be misleading. It was originally used because this section introduces the initial LES results before applying further analysis techniques. To avoid confusion, the section has been renamed to 'Mesh sensitivity analysis and wake flow characterisation', which more accurately reflects the content (line 245).

19. *Figure 3, Why did the authors pick the mesh #2 for the analysis of results? It does not feel like the mesh is fully converged, as differences are observed in the wake width and in the velocity profile at the edges of the wake (about 0.5D). Did the authors also check what fraction of turbulence was solved by the LES approach in the wake with the selected mesh, verifying Pope's criterion?*

Response: The authors have modified section 3 to address the concerns regarding mesh convergence and spatial resolution. First, the convergence study was extended to 4D, 6D, and 8D downstream of the AD. The updated Figure 3 and the text in lines 255–259 now demonstrate that Mesh #2 achieves a consistent behaviour across the entire wake width at these distances, showing excellent agreement with the finer meshes in the centre of the wake. While minor discrepancies persist in the high-gradient shear layer at the very edges,

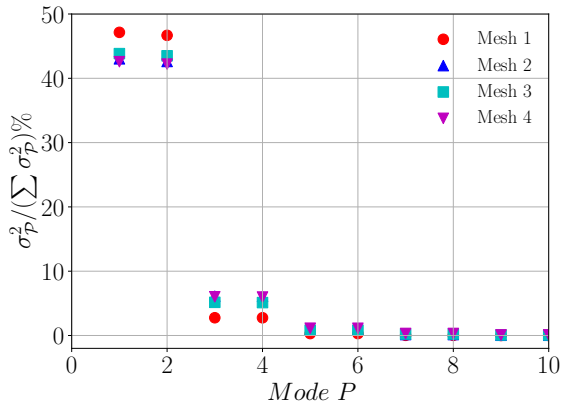

Figure A.1: Comparison of the energy fraction assigned to the POD modes associated with the vortex ring structure across the four different meshes (laminar inflow conditions, $S_t = 0.32$).

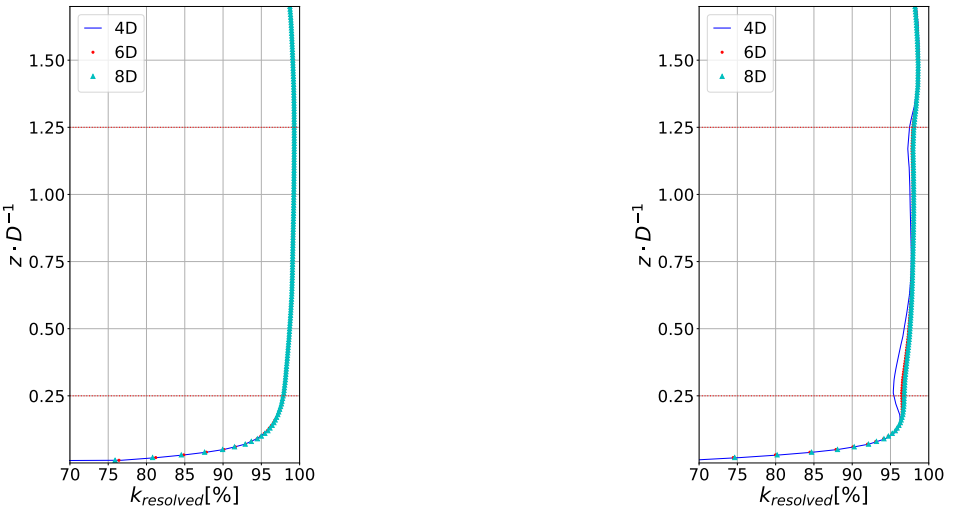

(a) TKE verification without AD

(b) TKE verification with AD

Figure A.2: TKE verification for ABL inflow conditions, without AD (a) and with the presence of AD (b), at 4D, 6D and 8D downstream the AD.

the overall resolution is sufficient to capture the relevant wake dynamics for this study. Furthermore, to ensure that the mesh resolution does not affect the identification of the dominant coherent structures, we performed a POD mesh sensitivity analysis. Fig. A.1 compares the POD analysis across the four meshes for the laminar inflow condition at $S_t = 0.32$. It can be observed that, starting from Mesh #2, the energy assigned to the modes linked to the vortex ring structure converges and is no longer affected by further grid refinement. This provides additional confidence that Mesh #2 is adequate for the analysis presented in this work. Additionally, Fig. A.2 shows the verification of Pope's criterion for the ABL case, confirming that the resolved turbulent kinetic energy (TKE) exceeds 95% of the total TKE in the wake region, both with and without the AD.

20. *Section 3, I wonder if the structure could be improved, as section 3 presents mostly the mesh-sensitivity analysis. Maybe the Q-criterion results be reported in a following section and Section 3 become something like "Mesh-sensitivity analysis"?*

Response: The authors have renamed Section 3 to 'Mesh sensitivity analysis and wake flow characterisation' to better reflect its content. Regarding the Q-criterion results, we have decided to keep them within this section as they provide the necessary qualitative transition between the mesh verification and the advanced POD post-processing in Section 4. Creating a separate section for the Q-criterion would result in a disproportionately short segment.

21. *Line 242, typo, "a converged statistics"*

Response: The authors thank the reviewer for identifying this error. The typo has been corrected to 'converged statistics' in the revised manuscript (line 300).

22. *Line 327, from the description of results, it is not clear from what result the authors draw a comparison between laminar and turbulent inflow conditions. As investigating the impact of different inflow conditions should be the focus of the analysis (as stated by the authors) the comparison between laminar and turbulent flows takes up a small part of the discussion. To highlight this comparison I wonder if the laminar results could be added to figure 13, at least for figure (c), highlighting differences in energy content, or if the comparison could be better shown in a different way. If the conclusions are drawn only from Figures 8 and 11, I find it interesting that, if I am not mistaken, in the laminar case the coherent pulsation of the first mode is amplified as it is convected downstream, while in the turbulent case it seems to be dissipated.*

Response: The authors appreciate this insightful comment. We have expanded the comparison between laminar and turbulent inflows to address these observations:

(a) Energy Comparison: As suggested, the laminar results have been added to Fig. 13 to provide a direct comparison of energy content. This highlights how background turbulence limits the energy retained by the vortex rings compared to the nearly 100% accumulation in the laminar cases.

(b) Spatial Evolution: We have clarified in the text that while coherent structures in the laminar case maintain their amplitude downstream, they indeed dissipate in the turbulent case due to the interaction with background turbulence and wake meandering.

These additions and the corresponding discussion can be found in the revised manuscript (Section 4, lines 396-407).

23. *Line 411, I wonder if the term wake meandering is adequate for the description of results with low inflow turbulence. In fact, looking at the arrows in Figure 19, it looks like the mode shows a clearly symmetric distribution around the centre line, which would suggest more a pulsation of the wake rather than meandering, with the wake expanding and contracting due to the rotor thrust oscillations.*

Response: The authors agree that modes 1-2 and 4-5 in Fig. 19 show a symmetric distribution corresponding to the wake's expansion and contraction (pulsation) due to thrust oscillations. However, the term 'meandering' is used to describe the behaviour of modes 3 and 6, which exhibit a non-symmetric spatial distribution. As shown in Figure 19, these modes display arrows pointing in directions that, when combined with their temporal evolution, result in a lateral oscillation of the wake.

24. *Figure 21, If possible, the size of the labels should be increased, as I find them particularly small.*

Response: The authors have increased the label size in Figure 21 to improve readability, as suggested by the reviewer.

25. *Line 451, looking at the laminar and low turbulence results of Figure 21 it might be worth highlighting that the intensity of the velocity oscillations is reduced for the turbulent inflow case.*

Response: The authors agree with the reviewer's observation. Section 5 (line 534) has been revised to highlight the diffusion in the intensity of velocity oscillations when moving from laminar to low-turbulence conditions, acknowledging the impact of background turbulence on the coherence of the wake structures.

26. *Line 470, I imagine that the authors want to highlight how for St=0.47, the half amplitude increases much faster, showing the peak value already at 3D. If this is correct, the sentence "except the highest frequency" might need further clarifying.*

Response: The authors agree. Section 5 (line 566) has been updated to clarify that for $S_t = 0.47$, the behaviour is similar to the laminar case, reaching its peak value at $3D$ followed by a continuous decay until $9D$.

27. *Line 470, from the description of the low-frequency results it seems that the onset of decay of the wake pulsation happens closer to the actuator disk than for the higher frequency cases. However, looking at results, the trend for the lowturbulence case seems opposite, as the velocity oscillation maxima gets closer to the AD with increasing St in Figure 22, b. I imagine the authors are referring to a faster decay in comparison to the laminar results of Figure 22, a. I would suggest clarifying this point for the reader by making the comparison with the laminar results explicit.*

Response: The authors have revised Section 5 (line 568) to make the comparison with the laminar case explicit. The text now clarifies that for lower frequencies ($S_t = 0.12 - 0.24$), the shift of the oscillation maxima towards the AD indicates an earlier onset of decay when compared to the laminar results, which is consistent with the lower energy levels observed in the POD analysis.

28. *Line 474, could the fact that the wake pulsation at these St numbers is unaffected by turbulence be correlated to the observed spectra in Figure 12 a and b? The wake spectra without motion shows a more significant frequency content for lower frequencies, which is then dampened out after about St=0.3, i.e, when the location of the peak seems not affected by turbulence.*

Response: The authors thank the reviewer for this insightful observation. While the frequency content in the background spectra (Fig. 12) suggests a potential correlation with the persistence of the wake pulsation near $S_t = 0.30$, a more detailed investigation would be required to confirm this link definitively, especially since in the case of ABL flow this pattern would not explain why all frequencies are affected with the exception of $S_t = 0.32$. This interesting point has been noted for future work.

29. *Line 494, "inclination towards the left" could maybe be improved to inclination in the negative x direction, or towards the AD or something else?*

Response: The corresponding paragraph has been entirely rephrased in the revised manuscript (Section 5, line 591). The terminology mentioned by the reviewer is no longer present in the updated text, which now provides a clearer description of the observed phenomena.

30. *Line 508, I wonder if it is correct to describe the wake as the superposition of pulsation and wake meandering. Indeed, if I am not mistaken, it seems to me like the observed wake meandering is due to the interaction between the wake pulsation and shear layer of the ABL, which deforms the pulsation in the vertical direction leading to the observed velocity patterns. In fact, was there vertical wake meandering in the fixed-bottom ABL case which could justify this comment? My idea would also fit with the following description proposed by the authors about the impact of different vertical advection velocities and the onset of wake meandering (line 520).*

Response: The authors have updated Section 5 (line 612) to describe the wake as exhibiting contraction and expansion coupled with a vertical deformation induced by wind shear. Regarding the reviewer's query, vertical meandering was already present in the fixed-bottom ABL case (without surge motion), confirming that the observed results under surge conditions represent a coupling between the forced pulsation and the pre-existing meandering.

31. *Figure 23, I wonder how this result combines with the ones in figure 21. In fact, there the authors described an inclination towards the left, while here the same conditions are seen as an inclination to the right (i.e., in the streamwise velocity). While I agree with the latter, I wonder if in Figure 21, we are actually observing an inclination to the left, or if the inclination is still towards the right, but the low-velocity zones are merging across different wake pulsations. In fact, in Figure 23, the shift of the wake pulsation in the bottom side of the wake is about 2D, matching the lines I have drawn in the Figure markup and the expected slower advection due to the ABL. Otherwise, If the authors do not agree with this explanation, how do they connect the different inclinations between Figure 23 and 21?*

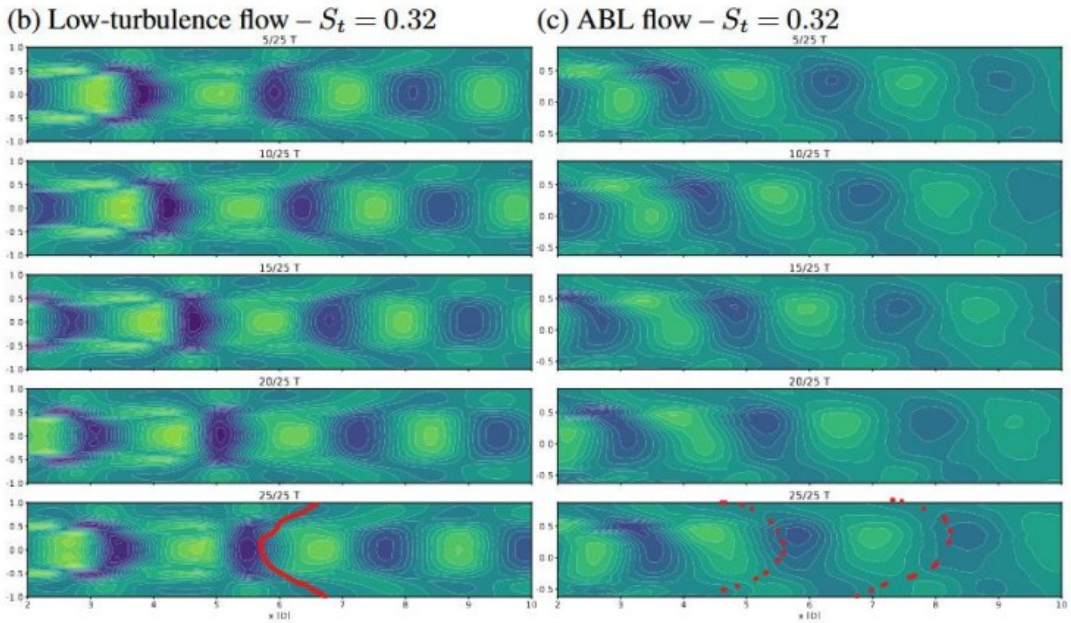

Response: The authors thank the reviewer for this observation. We agree with the as-

sessment and have re-evaluated the description of Figure 21 to ensure consistency with the physical evidence presented in Figure 23. To clarify that this complex pattern is likely caused by the merging of flow regions rather than a physical upstream tilt, the text in Section 5 (lines 544-555) has been revised as follows:
"Regarding the structural patterns, in both the laminar and low-turbulence cases, the regions of minimum fluctuation along the AD centreline appear to merge with off-centre zones, forming an upstream-facing curvature (towards the left) in the near wake ($x < 5D$). Further downstream, this pattern seems to invert into downstream-facing arcs. This behaviour could be attributed to the difference in advection velocities inside and outside the wake, a hypothesis that will be thoroughly analysed in the subsequent subsection. In the ABL scenario, the lower-fluctuation structures initially exhibit a downstream tilt up to $x \approx 4D$, likely resulting from the reduced advection velocity below the centreline caused by the shear flow. Beyond this point, an apparent sudden shift in inclination occurs, which may be caused by the merging of a low-velocity region from one structure with the subsequent one. Given the complexity of these flow features, they will be examined in greater detail and with clearer visualisations in the following subsection."

32. *Conclusions, Do the authors believe that the AD model can provide similar results to an actual three-bladed turbine model when describing the formation of coherent vortex structures? In fact, for a three bladed turbine under surge motion, the helical tip vortices, which are not captured in an AD model, might impact the behaviour of the vortex ring coherent structures. A comment should maybe included in the manuscript to highlight possible limitations of this study and/or future work.*

Response: The authors agree that while the AD model is robust for far-wake analysis, it cannot capture the discrete helical tip vortices or their initial breakdown. We have added a comment in the Conclusions (Section 6, lines 677-684) highlighting this limitation. This section now explicitly suggests that future work should utilise Actuator Line Models (ALM) or blade-resolved simulations to investigate how these helical structures transition and interact under realistic ABL conditions.

Comments from Reviewer 2

- *The main contributions should be more clearly articulated in the abstract and introduction to better guide the reader and emphasize the novelty of the work.*

  Response: As suggested, the Abstract and Introduction have been revised to more clearly articulate the main contributions and novelty of this work. Specifically, the Abstract now emphasizes three key findings:

  1. Energy-Frequency dependence: The identification of specific Strouhal numbers ($S_t = 0.30$ and 0.32) where the vortex ring structures reach maximum energy across different inflows.
  2. Meandering Coupling: The discovery that surge-induced structures and meandering act as decoupled phenomena in low-turbulence flows, but become actively coupled under ABL conditions due to the interaction with shear flow.
  3. Directional Decoupling: The observation that vertical and lateral meandering in ABL conditions rely on distinct physical mechanisms, with lateral meandering being independent of the vortex ring structure observed in the present study.

4. Inclined structures: The inclination of the structures present in the wake due to gradients in the advection velocity under ABL flow.

- *The rationale behind the selection of the simulated cases should be explained in greater detail.*

  Response: The rationale behind the selection of the simulated cases has been expanded in Section 2.4 (lines 233-245). Specifically, we have added a detailed explanation of how the chosen cases relate to previous experimental campaigns, while establishing a link between these parameters and the operational conditions of modern large-scale turbines (10–15 MW).

- *A brief introductory description of the data analysis techniques employed would improve accessibility for readers who may not be specialists in these methods.*

  Response: The authors agree that a more detailed introduction to the data analysis techniques enhances the manuscript's accessibility. Accordingly, Section 4.1 (POD - Laminar) has been extended to provide a clearer framework for interpreting the Proper Orthogonal Decomposition results.

- *Further clarification is needed regarding the validity and representativeness of results obtained using an actuator disk model at model scale, particularly in relation to full-scale, bladed wind turbines.*

  Response: The authors have addressed the validity and limitations of the AD model in both the Introduction and Conclusions. The AD model is a well-established and robust tool for investigating far-wake evolution and the global impact of platform motion. Furthermore, the surge motions investigated in this study are characterised by a Strouhal number (based on the rotor diameter) below $S_t = 0.5$. In this regime, the primary aerodynamic interactions are expected to occur at the global rotor scale rather than at the individual blade or tip-vortex scale. Nevertheless, we explicitly acknowledge that the AD approach bypasses the generation and breakdown of discrete helical tip vortices. The revised text clarifies that while the fundamental surge-induced modulation remains consistent, future studies using Actuator Line Models (ALM) or blade-resolved simulations are necessary to explore the near-wake interactions of these helical structures under realistic ABL conditions.

General Comments

- *Section 2.4 – Cases Analysed. I recommend adding a brief discussion linking the selected Strouhal numbers (St) to the characteristic frequencies of floating wind turbines in the 10–15 MW range. When combined with near-rated wind speed conditions, the St values considered in this article are expected to correspond to the frequency range associated with the rigid-body modes of spar or semisubmersible platforms. Providing this context would help readers better understand the physical relevance of the selected cases. In addition, it would be useful to clarify why higher reduced frequencies (potentially representative of the wave frequency range, where large platform motions may occur due to wave excitation) were not considered.*

Response: The authors agree that providing a physical context for the selected Strouhal numbers is essential. As suggested, Section 2.4 has been expanded to link the S_t range (0.12–0.47) to the natural frequencies of 10–15 MW spar and semisubmersible platforms (0.005–0.05 Hz). In addition, we have specified that higher frequencies ($S_t > 0.5$), typical of first-order wave excitation, were excluded to focus strictly on the low-frequency, large-amplitude dynamics. Furthermore, at these higher Strouhal numbers, the relevant aerodynamic interactions occur predominantly at the blade scale (such as tip vortex dynamics). Investigating these high-frequency motions would therefore require more detailed approaches, such as Actuator Line Models (ALM) or blade-resolved simulations, rather than the Actuator Disk model employed in this study.

- *Section 4. The presentation of the POD results could be made more didactic to benefit readers who may not be familiar with this type of analysis. For instance, further explanation could be provided on why certain modes appear as opposite pairs and how they should be physically interpreted. This is particularly important given the paper's structure, in which similar types of results are presented repeatedly for different cases. I recommend including a concise introductory explanation of how to interpret POD results, either at the beginning of Section 4 or by using the results in Section 4.1 as a guiding example, to support the reader throughout the remainder of the section.*

  Response: The authors agree that a more didactic approach to the POD results is beneficial. Following the reviewer's recommendation, Section 4.1 (POD - Laminar) has been significantly expanded to serve as a guiding example for the rest of the manuscript. We have included a detailed explanation of the physical interpretation of POD modes, specifically addressing why they often appear as opposite pairs (sine/cosine phases) to represent convective downstream motion of coherent structures. By establishing this framework in the first subsection, we hope to provide the reader with the necessary tools to interpret the more complex cases (low-turbulence and ABL) presented subsequently.

- *L512: "this phenomenon ... of the wake". I consider this one of the most interesting findings of the study, and it deserves greater emphasis in both the abstract and the conclusions. The result appears to be relevant to any situation in which the free-stream inflow is non-uniform, which broadens its potential impact.*

  Response: The authors appreciate the reviewer's positive assessment of this finding. We agree that the tilt of the wake structures due to the vertical gradient in advection velocity is a key contribution that extends to broader non-uniform inflow scenarios. As suggested, this phenomenon has been given greater emphasis in both the Abstract and the Conclusions.

- L560: *"the present study ... in previous experiments". This statement would benefit from further clarification. It would be helpful to more explicitly explain the relationship between the present results and those reported in previous experiments, highlighting similarities, differences, and possible reasons for any discrepancies.*

  Response: The authors have clarified the relationship between the current findings and previous experimental work in both Section 5.1 (lines 603–607) and the Conclusions (lines 671–672).

Specific Comments

- *Abstract: The abstract is long. I recommend shortening it to focus more clearly on the innovative aspects of the work and the most significant results.*

  Response: The Abstract has been shortened and restructured to focus exclusively on the study's innovative aspects and most significant findings, as recommended.

- *L2: "due to mooring lines": The motion is more directly related to the high compliance of the floating foundation rather than to the mooring lines alone. Please consider clarifying this point.*

  Response: The text in the Abstract (line 2) has been corrected as suggested.

- *L30: "movements": Please specify whether these are rigid-body motions or motions associated with the overall platform response.*

  Response: The term has been specified as 'rigid-body motions' in the Introduction (line 28).

- *L33: "by the surge frequency": Quasi-static effects are not dependent on the motion frequency. Rather, they are driven by the apparent wind speed experienced by the rotor, which is induced by platform motion regardless of its frequency. I suggest revising this statement accordingly.*

  Response: The statement in line 32 has been revised to clarify that quasi-static effects are driven by the induced apparent wind speed resulting from platform motion, rather than the motion frequency.

- *L59: "this structure": It is not clear what "the structure" refers to. Please be more specific.*

  Response: The text in line 58 has been updated to explicitly specify the 'vortex ring structure', clarifying the previous ambiguity.

- *L101: "data": Consider replacing "data" with a more precise term, such as "measurements of velocities" or another description that clearly specifies the type of data used.*

  Response: The term 'data' in line 100 has been replaced with 'streamwise velocity measurements obtained experimentally' to provide more technical precision.

- *L203: "10s are left . . . following 40s": How do these time intervals relate to full-scale conditions? Providing this information would be valuable, particularly for readers interested in applying a similar methodology to full-scale turbine simulations rather than a small-scale experimental setup.*

  Response: The relationship between experimental and full-scale time intervals has been added to line 253. The text now specifies that, based on a time scaling factor of 150, the intervals correspond to approximately 25 minutes of initialization and 100 minutes of data collection at full scale.

- *L204: "4D": Why was 4D selected? Are the results obtained at 4D representative of other downstream distances? Please clarify.*

  Response: While 4D was initially selected to maintain consistency with previous experiments, the study has been broadened to ensure the results are representative of the entire wake. Accordingly, Section 3 and Figure 3 have been updated to include the mesh independence study at 4D, 6D, and 8D.

- *L213: "Then, the two mesh refinements ... are recorded": The simulation procedure is not entirely clear. Please clarify whether this refers to a single continuous simulation with successive mesh refinements or to multiple separate simulations that were later combined.*

  Response: The simulation procedure has been clarified in lines 267–271.

- *L221: "experimental values": Please make explicit that the experimental results were used as the reference or target for the simulation setup.*

  Response: It has been made explicit in line 275 that the experimental results served as target for the validation and calibration of the simulation setup.

- *L242: "a vertical plane": It seems that multiple vertical planes may have been considered. If so, please use "vertical planes," or clarify that the same analysis is applied to several planes.*

  Response: To clarify, the POD analysis in the first sections is performed using several snapshots (time instances) but all within the same single vertical plane. The study then repeats this procedure for a horizontal plane in Section 4.4.

- *L527: "new": Please clarify in what sense this is "new" (e.g., new methodology, new physical insight, new configuration, or new application).*

  Response: The term has been clarified in the Conclusions (lines 632–634) to specify that the 'new' aspects refer to new physical insights regarding the vortex ring structure.

Comments from Reviewer 3

Specific comments

1. *L159, "The porous disk is assumed to have a constant CT". In my opinion, this assumption is correct in the case of a fixed inlet velocity and a still platform, but not so strictly in the cases analysed in the paper, since the relative velocity of the disk changes together with the platform motion. Perhaps the authors have previously observed that such changes do not come with a significant change in the value of CT. If this is the case, I suggest adding a brief explanation to strengthen the validity of the assumption. Furthermore, a discussion of a possible loss of generality (if any) when extending results of an actuator disk to a three-bladed rotor would help clarify the applicability of the framework presented in the paper.*

Response: The authors thank the reviewer for this observation. The assumption of a constant C_T has been clarified in Section 2.2 (lines 168–178). We explain that while surge motion induces variations in apparent wind speed of approximately $\pm 25\%$, experimental data from Aubrun et al. (2019) confirm that the aerodynamic drag of the rigid porous mesh remains stable within this Reynolds number range. Additionally, we have added a discussion acknowledging that while this approach isolates the kinematic interaction between the motion and the wake, it does not account for the C_T variations (pitch control, tip-speed ratio) typical of a real three-bladed rotor. Furthermore, we have extended the discussion regarding the limitations of the AD approach in both Introduction and Conclusions.

2. *The choices described in section 2.3 regarding the dimensions of the computational domains should be clarified more in details. For example, if the intent is to compare experimental and numerical results to obtain a validation, it is not clear why the dimensions of the domain are smaller than those of the wind tunnel. Also, clarifications should be required to support the choice of a 5D height for the ABL domain, as well as for the use of different boundary conditions for the top and bottom walls.*

   Response: The details regarding the computational domain and boundary conditions have been expanded in Section 2.3. Specifically:

   (a) Domain Dimensions and Blockage: We clarify that the domain cross-sections result in a blockage ratio of less than 1% for uniform flows and 1.5% for the ABL case. Both are well below the 5% threshold where confinement effects become significant (Sarlak et al., 2016), ensuring that the smaller numerical domain (relative to the physical wind tunnel) does not introduce artificial acceleration.

   (b) Domain Height (5D): The choice to limit the height to $5D$ in the ABL case is justified as a strategy to model the Atmospheric Surface Layer (ASL). This prevents the artificial decay of turbulence that occurs in deep domains without temperature-driven inversion layers.

   (c) Boundary Conditions: We have clarified the use of stress boundary conditions for the ABL case. A Schumann's model is applied to the bottom to represent surface roughness, while a top shear-stress condition (based on friction velocity u^*) is used to provide the necessary forcing to maintain the turbulent profile within the truncated domain.

3. *Section 2: The dinstinction between the three conditions is appreciated and essential to understand the following of the paper, including section 2.3 for instance. IS shear considered in the low turbulence case?*

   Response: It has been clarified in line 222 (and further detailed in Section 2.3) that the low-turbulence case does not include shear. The targeted mean flow for this case is entirely uniform, with only the turbulent fluctuations superimposed on the signal.

4. *The conclusions drawn from the mesh convergence study presented in section 3 may be leave room for discussion, as the mesh #2 does not seem to be fully converged (for example in the shear layer between 0.75 and 0.25 D). Furthermore, demonstrating the level of convergence of more than one section downstream would help to provide a stronger generality to the conclusions of the convergence study.*

Response: The mesh convergence study in Section 3 has been expanded to address these concerns. We now include wake profiles at 4D, 6D, and 8D downstream of the AD to demonstrate the generality of the results. The updated text clarifies that while minor differences exist in the high-gradient shear layer, Mesh #2 shows consistent behaviour and strong agreement with the finer meshes in the centre of the wake at all three locations, confirming that the spatial resolution is adequate for the study's objectives. Furthermore, to ensure the robustness of our primary methodology, we conducted an additional POD mesh sensitivity analysis. As illustrated in Fig. A.1 (page 5 of this document), the energy assigned to the modes associated with the vortex ring structure (evaluated under laminar inflow conditions at $S_t = 0.32$) converges from Mesh #2 onwards. This confirms that the selected grid resolution accurately captures the coherent structures driving the wake dynamics without being affected by further refinement.

Technical corrections

Response: All technical corrections listed below have been addressed and incorporated into the revised manuscript.

1. *L3, possible typo, I think "has been the subject of study" would sound better.*
2. *L4, possible typo, I think "as most studies" would sound better.*
3. *L10, typo, "with the highest energy at Strouhal numbers30 and 0.32, respectively".*
4. *L54, typo, "... six degrees of freedom... ".*
5. *L60, typo, "Due to these reasons".*
6. *Figure 4 caption, typo, "All profiles are zoomed in the refined region. The dotted red... ".*
7. *L260, typo, "see Table 2".*
8. *L260, possible rephrasing for improved clarity, i.e. "In all figures, the most energetic modes include pairs with similar energy content".*
9. *L283, possible rephrasing, "ST = 0.32 exhibits higher energy in the first pair of modes and lower energy in the harmonics".*
10. *L310, please rephrase "The range of frequencies in these modes, not shown here, are a great match with... " or correct the verb "are" with "is".*
11. *L339, typo, "mode pairing".*
12. *L391, typo, "This comprehensive comparison with laminar and low-turbulence inflows has revealed ... "*
13. *L395, perhaps "ABL inflow conditions" sounds better than "ABL flow".*
14. *L444, typo, "the local mean velocity is subtracted" or "the local averaged velocity is subtracted".*
15. *L503, typo, "... due to the surge motion".*
16. *Coherence should be maintained with British or American English, since in the manuscript terms like visualise/visualize or analyse/analyze are present at the same time. The same applies to the terms disc/disk.*

Comments from Reviewer 4

General

- *The study is obviously designed in a way that the experiments of Schliffke et al. could be reproduced. However, no comparison with their results has been performed, which is quite surprising. Please explain in the paper, why this is the case and why you still choose to replicate the rest of the setup. I guess this is due to the fact that Schliffke et al. Considered a Ct of 0.5, which is rather low. However, at least a short validation case with Ct=0.5 and a comparison with the experimental data would be very beneficial. This uncertainty (what is actually replicated here and why?) remains through the paper and should be clarified to strengthen the red line of the study. It is also very important to discuss the chosen motion conditions. They have been adapted from Schliffke, however, according to my understanding, they represent a rather small 2MW rotor at very slow motions (between 100 and 16s of motion period at 8m/s) and quite large motion amplitudes (12.5% of the rotor diameter). The chosen motion parameters should be set into the context of modern turbines.*

Response: The authors thank the reviewer for these insightful comments, which have led to significant clarifications in Section 2:

1. Replication vs. Validation: We have clarified that while the study adopts the geometric scale, inlet profiles, and motion parameters of the experimental campaigns, its primary goal is not a direct quantitative validation. Instead, it uses this well-characterised setup as a physically realistic reference framework to isolate and analyse fundamental wake dynamics under controlled conditions (Section 2, lines 119-122).

2. Thrust Coefficient (C_T): We particularly appreciate the reviewer's observation regarding the C_T value. While previous literature (Schliffke et al., 2024) mentioned a $C_T = 0.5$, it was confirmed to be 0.65. This discrepancy was addressed with the experimental authors, leading to an official corrigendum in the respective journal (doi:10.5194/wes-9-519-2024-corrigendum). Our study correctly uses $C_T = 0.65$ to match the experimental measurements of the porous disk (Aubrun et al., 2019), as now detailed in Section 2.2.

3. Context of Modern Turbines: We have added a dedicated discussion in Section 2.4 regarding the scaling of the motion parameters. Although the original experiments were based on a 2 MW turbine, the analysed Strouhal numbers ($S_t = 0.12$ to 0.47) correspond to the natural frequencies (0.005 Hz to 0.03 Hz) and rigid-body motions of modern 10 MW to 15 MW floating turbines. The motion amplitude of $D/8$ is justified as a bounding scenario for extreme resonant responses in these large-scale structures.

Abstract

- *The abstract is comparatively long and it is recommended to make it shorter. The description of the simulation study is quite detailed for an abstract, however, still difficult to follow since it seems that the authors try to explain the complete study in detail here. It is recommended to reduce the level of detail and focus on the basic idea of the simulation study and the main findings, while leaving out how this was achieved. It would be beneficial to move a bit more towards a bird's eye perspective.*

Response: The abstract has been significantly condensed as suggested. We have reduced the technical procedural details of the simulation and focused the text on the core objective and the most significant findings.

Introduction, numerical modelling and experimental studies

- *A number of relevant publications in the field are listed and described here. However, only very few conclusions relevant for this study are drawn from the description. It would be beneficial to really discuss some of the studies in the context of the present work. For example, the role of the motion frequency is not really discussed. The suitability or limitations of the used method could also be discussed using the literature.*

Response: The section of the Introduction regarding the numerical modelling of FOWT wakes has been specifically rewritten to address the reviewer's request for a deeper discussion of existing literature. The new paragraph now discusses the role of motion frequency and justifies the use of the AD methodology.

Solver

- *It is written that "a newly implemented solver in OpenFOAM (OpenCFD-Ltd, 2004), which was constructed using the SOWFA libraries as a basis (Churchfield et al., 2012a, b)" was used in to perform the simulations. First: Is this an in-house development? If yes: Please either describe the implementation or give a source. What is implemented and how is it verified? What part is taken from other sources and what is the own contribution? If no: Please give a source, where the actual implementation is described. If you use the SOFWA code, the version of the code should be named and the source for the actual implementation should be cited (at least the github repository).*

Response: The description of the numerical solver has been clarified to specify that it is based on the standard SOWFA libraries (NREL, 2012; Churchfield et al., 2012a, b), effectively utilizing its well-verified core framework. We have made explicit that our implementation introduces only two specific modifications to the standard code:

1. Simplified Physics: Temperature variations and buoyancy effects were disabled to focus exclusively on the fluid mechanical behaviour.
2. Adapted Driving Mechanisms: We modified the forcing to suit different inflow cases. For the ABL, a forced pressure gradient is calculated based on a precursor region (restricted to hub-height velocity to avoid bias from the wake), while the laminar and low-turbulence cases are driven by inlet boundary conditions (fixed velocity or filtered noise) rather than a pressure gradient.

The github repository for the utilised version is included in the citation.

Inflow conditions

- *A discussion on the chosen ABL parameters is missing: Is there only one ABL? What is special? What is chosen and why?*

Response: The physical characteristics of the chosen ABL have been clarified in Section 2.3 (lines 226–230), where we specify that the flow is modelled to replicate the scaled wind tunnel boundary layer from the experimental study by Schliffke et al. (2024) rather than a specific geographic site. To ensure a physically realistic and reproducible setup, the target velocity and turbulence intensity profiles were configured following the VDI guideline 3783 for atmospheric

boundary layer wind tunnel modelling. This configuration was selected to provide a standardised, strongly sheared, and highly turbulent baseline, which is essential for establishing a clear contrast with the uniform, non-sheared inflow cases and thus isolating the impact of ABL-specific features on the wake dynamics.

POD laminar

- *"Furthermore, the frequencies exhibited in the modes, as illustrated in Fig. 9a, show a smooth distribution across a range of frequencies. Additionally, modes 3 and 4 display a complementary spectrum when compared with modes 1 and 2. Modes 5 to 10 (not shown here) also demonstrate analogous complementary behaviour with regard to frequency. This finding suggests that the observed structure is inherent to all frequencies within a range, thereby confirming the absence of any structure being advected that can be associated with a specific phenomenon."*
  This seems a bit inconsistent to me. Actually, Figure 8 shows clear structures in modes 1-4. The corresponding Fourier spectra actually show that there is not one isolated frequency associated with the modes, however, the range of corresponding dominant frequencies is rather narrow (St 0.2-0.55), and far from being distributed randomly. Therefore, I cannot really follow, why there should be an "absence of any structure being advected that can be associated with a specific phenomenon". The fact that this structure seems to be rather weak (6 magnitudes smaller) seems convincing on the other hand. However, when summing up the Fourier amplitudes in a range of St e [0.2-0.55], I would expect to see a similar (or even higher) value compared to the other two cases. Let's assume that there are structures generated in case of St=0; however, these structures would be related to some kind of "natural" meandering or sth. similar. In this case, the structures would not necessarily evolve at the exact same frequency, since their generation is somehow of a statistical nature. As known from other studies, such meandering should be pronounced around St 0.3. In this case, the assumed structures in the wake would be present, however, their frequency and lateral expansion would slightly vary over time. A Fourier transform on this (let's say for a time of 40s), would actually not show a clear peak, but more a stochastic distribution around St 0.3. From my point of view, this could be in line with what we see in Figure 9a. If this is true, we would actually have some stable structures in the wake. which slowly vary their frequency. However, due to the long window of time, we cannot exactly see them in the POD analysis, since it requires the structures to happen at the EXACT same frequency and lateral expansion.

Response: The authors are very grateful for the reviewer's insightful reflection on the frequency distribution for the $S_t = 0$ case. We agree that a broadband spectrum in the range of $S_t \approx 0.2$–0.55 could indeed suggest physical mechanisms whose frequency and spatial expansion evolve statistically over time, such as wake meandering. However, as the reviewer correctly noted, the energy content of these modes is extremely low (six orders of magnitude smaller than the mean field). Furthermore, the spatial modes remain strictly symmetric, which is inconsistent with the typical alternating patterns of meandering. Consequently, while we have incorporated the reviewer's observation into the text to acknowledge the possibility of evolving structures in lines 335-342, we conclude that these represent negligible residual fluctuations rather than dominant coherent phenomena.

POD turbulent

- *For the St=0 case, the maximum frequency of Mode 1 occurs somewhere around 0.075Hz, which is far from the maximum frequency observed in the laminar case. Does this frequency somehow relate to the turbulence length scale of the low turbulence case (6D)?*

Response: The authors appreciate this detailed observation regarding the spectral peak in the low-turbulence case for $S_t = 0$. We have carefully reviewed the relationship between the peak frequency and the turbulent length scale ($L_x \approx 910$ mm). It is important to note that the figures are presented in terms of the Strouhal number (S_t) rather than absolute frequency. For an inlet velocity of $U_{ref} = 2.71$ m/s and a disk diameter of $D = 0.16$ m, the peak mentioned by the reviewer at $S_t \approx 0.075$ corresponds to a frequency of approximately 1.27 Hz. On the other hand, the characteristic frequency associated with the longitudinal turbulent length scale ($f_L = U_{ref}/L_x$) is approximately 2.98 Hz, which yields a $S_t \approx 0.17$. While these values do not coincide exactly, they are within the same order of magnitude. This suggests that the energy distribution in these modes is indeed influenced by the scales of the incoming turbulence, possibly linked through harmonic interactions or the spectral decay of the low-turbulence inflow.

Phase averaging

- *I understood that the phase averaging in Fig 21 was performed at the motion frequency (St=0.32). Is this correct? If yes, I would expect a behaviour in Fig. 21 (a), which is somehow similar to modes 1 and 2 in Figure 8 (c), since those occur at the exact same frequency. However, in Fig 21 (a), the distance in downstream direction between minima and maxima of the pulsation is approximately twice as high, which indicates a much lower frequency (half the motion frequency?). Maybe I am getting something wrong here. It would be helpful if you could explain this.*

Response: The reviewer is correct that the phase averaging was performed at the motion frequency ($S_t = 0.32$). The perceived difference in the spatial wavelength between Fig. 21(a) and the POD modes in Fig. 8(c) is due to the physical quantity being represented. While the phase-averaged fields in Fig. 21(a) show the streamwise velocity component, which includes the sign of the fluctuations, the POD spatial modes in Section 4 are based on the velocity magnitude. We have added an explicit clarification in line 538 to ensure the reader understands this distinction.

Conclusion

- *"Overall, the study highlighted that the vortex ring structure exhibits a significantly different behaviour depending on the inflow conditions. In particular, the presence of ABL shear not only modifies the spatial shape of the modes but also strongly influences their amplification and energy distribution."*
  From my point of view, this has not been shown directly. I guess, the fact that the "ABL shear ... strongly influences their amplification and energy distribution" is derived from Figure 12 (a-c). Here, it is shown that the amplification strongly changes from the low-turbulence to the ABL case. However, the difference between the low-turbulence to the ABL flow is not only the ABL shear, but also a significant increase of the overall turbulence level. Therefore, I would not be able to distinct if the shear or the increased level of turbulence caused this.

Response: The authors agree with the reviewer's observation. In our original text, we attributed the observed changes primarily to the ABL shear, whereas the transition from the low-turbulence case to the ABL case involves both the introduction of shear and a significant increase in the background turbulence intensity (TI from $\approx 1.2\%$ to $\approx 9\%$). It is indeed the combination of these two factors that drives the differences in wake modulation and energy distribution. We have revised the Conclusions (line 680).

Influence of the inflow conditions on the dynamics of a floating wind turbine wake under harmonic surge motion

Dimas Alejandro Barile[1,2], Roberto Sosa[1,3], Sandrine Aubrun[4], and Alejandro Daniel Otero[1,2]

[1]Universidad de Buenos Aires, Facultad de Ingeniería, Av. Paseo Colón 850, Buenos Aires, C1063ACV, Argentina
[2]CONICET, Centro de Simulación Computacional para Aplicaciones Tecnológicas, Godoy Cruz 2390, Buenos Aires, C1425FQD, Argentina
[3]CONICET - INTECIN, Av. Paseo Colón 850, Buenos Aires, C1063ACV, Argentina
[4]Nantes Université, École Centrale Nantes, CNRS, LHEEA, UMR 6598, F-44000 Nantes, France

Correspondence: Alejandro Daniel Otero (aotero@fi.uba.ar)

Abstract. Floating Offshore Wind Turbines (FOWTs) are projected to undergo substantial expansion in the coming decades. However, the high compliance of their floating foundations, coupled with aerodynamic, hydrodynamic, and mooring forces, leads to complex platform motions that ~~the motion of their supporting platforms due to mooring lines and wave interaction~~[rev] make it difficult to predict their wake dynamics. The vortex ring structure produced during surge motion has been the[rev] subject of study for nearly a decade now but there are still many features to bring to light. As most ~~of the~~[rev] studies have been under idealised, uniform flow there is little knowledge on how this structure behaves under Atmospheric Boundary Layer (ABL) flow. In this work, the authors propose to study this structure under three different inflow conditions: laminar and low-turbulence uniform flows, and ABL flow. Large Eddy Simulations are carried out in combination with an Actuator Disk (AD) as a wind turbine model, with a focus on surge motion and a Strouhal number ranging between 0 and 0.47. The velocity values are extracted at a vertical plane parallel to the AD axis, which is subsequently analysed by means of Proper Orthogonal Decomposition (POD) and phase averaging. In the POD analysis, vortex ring structures are identified under all inflow conditions, though their energy decreases as turbulence increases. Additionally, a dependence of energy on frequency is observed for low-turbulence and ABL flows, with the maximum energy occurring at Strouhal numbers 0.30 and 0.32, respectively. Furthermore, vertical meandering is detected in both cases. In low-turbulence, meandering and vortex rings act as decoupled phenomena. Replicating the analysis on a horizontal plane at hub height, it is observed that lateral meandering is uniformly intense under this inflow condition. Conversely, under ABL conditions, the surge motion interacts with the turbulent shear flow to actively induce a coupled vertical meandering. Vertical and lateral meandering in ABL conditions rely on entirely distinct mechanisms, the latter being unrelated to the vortex ring structure. Finally, phase averaging analysis indicates that the wake is modulated by the surge motion, manifesting as expansions and contractions, for laminar and low-turbulence cases. Conversely, an inclination of the structures towards the flow direction is identified in the ABL conditions, attributable to the shear flow.[rev]

1 Introduction

In the global pathway towards decarbonization, wind energy has taken the place as one of the leading renewable technologies over the past decades. As shallow-water sites become increasingly saturated, floating offshore wind turbines (FOWTs) are expected to play a central role in the expansion of wind power into deeper waters (Zhou et al., 2025). However, the knowledge gained from bottom fixed wind turbines still leaves several open questions when extrapolated to floating configurations ~~the latter~~[rev], since in addition to aerodynamics, hydrodynamics and mooring now also play a significant role. FOWTs are subjected to rigid-body motions in six degrees of freedom ~~6 degrees of freedom movements~~[rev], which lead to an overall modification in both aerodynamic performance and wake structure formed downwind. It was first described by Xu et al. (2015), Farrugia et al. (2016), Tran and Kim (2016) and Wen et al. (2017) that wind turbines subjected to periodic surge movement show oscillations on thrust and power output, as the blades experience variations on local angle of attack. Schulz et al. (2024) define these as quasi-steady~~quasi-static~~[rev] effects, as they are driven by the instantaneous apparent wind speed experienced by the rotor due to the platform motion~~regulated by the surge frequency~~[rev]~~, while there are also other unsteady phenomena occurring at the blades~~[rev]. Also, it has been pointed out that, out of all possible movements, wind turbine aerodynamics are mostly affected by turbine surge and pitch motions (Lee and Lee, 2019; Wang et al., 2023). In terms of wake modifications, surge motions generate a pulsating mode in the form of periodic expansion and contraction in the wake, which have been studied for the past decade both numerically and experimentally (Sivalingam et al., 2018; Messmer et al., 2024; Hubert et al., 2025).

In the numerical modelling of FOWT wakes, simulations using the Actuator Line Model (ALM) have consistently shown that surge motion induces a transformation of standard helical tip vortices into distinct, stronger vortex ring structures (Arabgolarcheh et al., 2023a, b; Wang et al., 2024). The formation and strength of these structures are heavily dictated by the platform's motion frequency, which directly governs the growth rate of vortex instabilities (Kleine et al., 2022). As demonstrated by Duan et al. (2022) using blade-resolved improved delayed detached eddy simulation (IDDES), the surge frequency governs the intensification of these vortex rings at specific intervals and has a significantly larger impact on the overall wake structure than the surge amplitude. While ALM and blade-resolved approaches are strictly necessary to resolve the discrete, transient helical tip vortices in the near-wake, the Actuator Disk (AD) model presents a highly suitable and computationally efficient alternative for studying the overall wake behaviour under surge motion. Although the AD approach inherently bypasses the resolution of individual blade tip vortices, it successfully captures the downstream symmetric vortex ring structures that dominate the interaction between surge motion and wake development. As pointed out by Kopperstad et al. (2020), the inherent symmetry of these rings makes the AD particularly appropriate for such far-wake analyses. This assumption is further substantiated by recent ALM studies (Zhou et al., 2025) which confirm that vortex rings formed under surge motion firmly retain their symmetry. Furthermore, the AD method has been reliably applied to demonstrate how surge-induced turbulence accelerates wake recovery (Rezaeiha and Micallef, 2021), thereby justifying its application for evaluating overall wake development under surge motion.[rev]

However, most of the aforementioned studies characterising these surge-induced structures~~Most of these studies~~[rev] were carried out under uniform, idealised flow conditions. This is a useful approach to isolate the particular phenomena present

in FOWT but it leaves out~~leaves away~~[rev] effects produced in Atmospheric Boundary Layer (ABL) flow. In particular, due to the continuing increasing size of wind turbines, there is a need for studies that can predict the effect of ABL flow over the vortex ring structure~~this structure~~[rev]. Also, ABL turbulence is responsible for wake meandering, which interacts with the wake dynamics produced by surge motion. Due to these~~s~~[rev] reasons, Xu et al. (2022) suggest the need for further investigations of more realistic atmospheric inflows and strong interactions between multi-FOWTs. In this line of work, Zhou et al. (2022) and Nybø et al. (2022) studied the effect of atmospheric turbulence on FOWT by means of synthetic turbulence generators, and in the case of Nybø et al. (2022) the results were compared with Large Eddy Simulations (LES), pointing out that synthetic models may lead to incorrect estimations for FOWT dynamic responses besides not considering ABL flow thermal stability. Johlas et al. (2019, 2020) conducted full ABL simulations incorporating the motions induced by waves on an ALM. The results demonstrated that, due to turbine pitch motion, the wakes of FOWTs exhibit an upward deflection in comparison to the wakes of fixed wind turbines. Also, Xu et al. (2023, 2024) studied full ABL flows combined with ALM by means of LES in the first case and DDES in the second. Results confirm previous findings for wake centre deflection under pitch motion and that, under ABL flow, platform motions have negligible impact on wake recovery. The latest work also includes a comparison with uniform and shear flows. In terms of vortex structures, they were able to visualise the tip vortices breaking apart into the ring structure for the uniform and shear cases but, due to the presence of other structures in ABL flow, the ring vortex structure is not distinguished in the wake for this case. Bridging this specific gap, namely understanding the persistence and behaviour of vortex rings generated by surge motion under realistic atmospheric turbulence and shear, constitutes the primary motivation of the present study.[rev]

Regarding the experimental approach, Messmer et al. (2024) studied a model wind turbine under laminar flow and surge motion, analysing a range of Strouhal numbers $S_t = \frac{f_{surge}\, D}{U_{ref}}$ between 0 and 1, where D denotes the disk diameter, f_{surge} the surge motion frequency, and U_{ref} the upstream reference velocity.[rev] Results show a clear pulsating structure on the wake for $0.2 \leq S_t \leq 0.55$, with the frequency of the motion appearing in the wake spectra. In terms of realistic inflow conditions, Schliffke et al. (2020, 2024) conducted experiments in an ABL wind tunnel with a porous disk subjected to surge motion and analysed the wake profile at 4.6D downstream. These experiments included a range of $0 \leq S_t \leq 0.36$. The authors observed that while harmonic motions leave a clear frequency signature in the wake's energy spectra, they do not significantly alter time-averaged statistics. Specifically, for a motion amplitude of $\frac{D}{8}$, in the second work they determined that a S_t number of at least 0.19 was required to detect this signature at a downstream distance of 8D, as almost no sign is detected for $S_t \leq 0.13$. Also, the higher signature was observed close to $S_t = 0.30$. In the context of the UNAFLOW campaign, Fontanella et al. (2021, 2022b)[rev] obtained analogous results regarding wake recovery ~~in an ABL wind tunnel~~[rev] by analysing the wake at 2.3D under uniform inflow conditions with~~in~~[rev] low TI ~~flow~~[rev]. Recently, Hubert et al. (2025) investigated the spatio-temporal nature of this effect achieving an experimental visualisation of the signature of the vortex ring structure under ABL flow by means of Particle Image Velocimetry (PIV). Even at a lower Strouhal number ($S_t = 0.11$), they described the wake's dynamic response as a pulsating behaviour, characterised by a periodic contraction and expansion of the wake rather than a displacement of its centre.

To successfully isolate these periodic structures from background turbulence, advanced analysis techniques are required.[rev] The Proper Orthogonal Decomposition (POD) method provides a decomposition basis for the data that is optimal in terms of energy as it sorts the resulting modes by energy content. It is useful in cases where certain structures have a specific frequency associated (Iungo et al., 2015), like the case of the vortex ring structure and surge motion. In VerHulst and Meneveau (2014); Hamilton et al. (2018); Ali et al. (2021) the method was applied to the wake obtained from LES combined with an AD, and in Andersen et al. (2014); Cherubini et al. (2022) with an ALM. In the latter, the frequency spectrum was calculated for each mode to have a better interpretation of the structures present. Bastine et al. (2014, 2015) applied this method considering a plane at 4D downstream an AD to visualise the modes under ABL flow. Regarding FOWT cases, Wang et al. (2024) applied the method downstream an ALM under surge motion and uniform inflow. The results show that 4 modes are enough to capture 95% of the energy in the wake. Also, in Raibaudo et al. (2022) the technique was applied to planes of streamwise velocity obtained experimentally ~~experimental data located~~[rev] at 4.6D and 8.1D downstream of a porous disk model under surge motion. For each case, the corresponding surge frequency was identified within the modes but no specific spatial mode was found.

As far as the authors are aware, there is still lack of studies that explain the effects of combining realistic ABL conditions with FOWTs phenomena. In this work, we expect to shed some light on this matter by comparing the flow structures produced by surge motion under three distinct inflow conditions: laminar uniform flow, low-turbulence uniform flow, and ABL flow. This progression allows us to systematically test the effects of background turbulence and vertical shear flow. LES are carried out together with an AD representing a FOWT model under surge motion. Different frequencies of surge motion are analysed, and the resulting wake for each case is studied using POD and phase averaging with the corresponding surge frequency. By applying these techniques, this study aims to characterise the spatial and temporal evolution of the pulsating structures and determine how they are modulated or disrupted by the atmospheric environment.[rev]

The paper will be organised as follows: the numerical setup is detailed in section 2. Section 3 presents the mesh sensitivity analysis and baseline wake flow characterisation.~~while the preliminary LES results are shown in 3~~[rev]. Then, the POD analysis is outlined in section 4, followed by the phase average study in section 5. Finally, conclusions are drawn in section 6.

2 Numerical Setup

The numerical setup is defined based on the wind tunnel located at École Centrale Nantes, where porous disks have been studied as wind turbine models for the past years under an offshore-like ABL flow (Schliffke et al., 2020; Belvasi et al., 2022; Schliffke et al., 2024; Hubert et al., 2025). With a 26-metre test section and a cross-section measuring 2 m by 2 m, this open-circuit atmospheric wind tunnel is set up to reproduce a neutral atmospheric boundary layer at a geometric scale of 1:500. The porous disk diameter is $0.16\ m$, resulting in a blockage ratio of approximately 0.5%,[rev] and in the case of ABL flow, the hub height is ~~considered at~~[rev] $0.12\ m$. While the present study adopts the same geometric scale, inlet profiles, and motion parameters as the experimental campaigns, its objective is not to perform a direct quantitative validation against a specific dataset. Instead, the experimental configuration is used as a physically realistic and well-characterised reference framework to isolate and analyse the fundamental wake dynamics under controlled inflow conditions.[rev]

Within this framework, three different inflow conditions are considered[rev]. The first one is a uniform laminar flow where the inlet velocity is unperturbed. Then, a second case is built with a perturbation on the inlet flow leading to a uniform low-turbulence flow, with a $TI \approx 1.2\%$. Finally, an ABL flow is considered with a higher turbulence, reaching $TI \approx 9\%$ at hub height. The mean velocity and turbulence intensity profiles will be presented in section 3. In the case of the ABL flow, the results presented herein build upon and substantially extend the preliminary findings reported in Barile et al. (2025). Through these three varying inflows, specific phenomenological similarities with the experimental observations are qualitatively compared later in sections 4 and 5.[rev]

2.1 Numerical model

The flow is governed by the spatially filtered incompressible Navier–Stokes equations, which are solved using the SOWFA libraries (NREL, 2012; Churchfield et al., 2012a, b) within the OpenFOAM framework (OpenCFD-Ltd, 2004). The subgrid-scale stresses are modelled using a one-equation eddy viscosity approach (Yoshizawa, 1986) for the ABL case, and a Smagorinsky formulation for the laminar and low-turbulence cases. The AD forces are included as source terms in the momentum equations.[rev]

While the core numerical framework follows the standard SOWFA implementation, two main modifications were introduced to suit the current study. First, temperature variations were disregarded, focusing solely on the fluid mechanical behaviour of the flow. Second, the driving mechanisms were adapted depending on the flow case. ABL flow simulations are driven by a forced pressure gradient. For this case, a precursor region is defined upstream of the AD where a specific reference velocity is forced at hub height. Only the average velocity at hub height in this region is taken into account to calculate the pressure gradient, which is then applied to the entire domain. This approach ensures that the forcing mechanism is not biased by the local flow perturbations induced downstream of the disk, while still maintaining the desired boundary-layer development. Conversely, the laminar and low-turbulence flow simulations are driven by an inlet boundary condition instead of a pressure gradient. In both cases, the same reference velocity value is set. However, in the low-turbulence case, a perturbation is added to achieve a low-turbulence inflow with length scales close to the ABL case, as described in section 2.3. In contrast, an unperturbed inflow is considered for the laminar case.[rev]

2.2 Actuator disk

To represent the effect of the porous disk an AD approach (Jimenez et al., 2007; Mikkelsen, 2004) is used, which is similar to the one presented in Navarro Diaz et al. (2019a, b, 2021). The AD is represented by a set of nodes arranged on a planar disk that are independent of the background fluid mesh. Nodes are arranged as rings and the separation between rings is set according to Navarro Diaz et al. (2023). To ensure numerical stability, the nodal forces are later spread to the surrounding cells through a regularization kernel, which relies on a three-dimensional Gaussian distribution (Porté-Agel et al., 2011; Hodgson et al., 2021).

First, a calibration table is constructed, for which the motionless AD is simulated with different fixed inlet wind speeds and uniform force distribution, in order to establish the induction relation between the unperturbed wind speed and the velocity at

each AD node. During the CFD simulation, the AD is subjected to a sinusoidal surge motion where the position and velocity are given by:

$$\Delta x(t) = A_{surge}\, sin(2\pi f_{surge}\, t), \tag{1}$$

$$\Delta v(t) = 2\pi f_{surge} A_{surge}\, cos(2\pi f_{surge}\, t). \tag{2}$$

In the above expressions, A_{surge} is the surge amplitude which is considered $D/8$ based on Schliffke et al. (2020, 2024) and f_{surge} the corresponding frequency, which differs across cases. Considering the fluid velocity at each node U_i, the local velocity sensed by the AD node is obtained in each time step as:

$$U_{i|rel}(t) = U_i(t) - \Delta v(t) \tag{3}$$

which is then used to enter the calibration table and obtain the unperturbed wind speed relative to the AD, $U_{\infty|rel}$. Finally, the force is calculated as:

$$\Delta f_i = \frac{1}{2}\rho\, C_t\, {U_{\infty|rel}}^2\, \Delta S_i, \tag{4}$$

where ρ is the air density, C_t is the disk thrust coefficient, ΔS_i is the area corresponding to the particular AD node. The thrust coefficient of the AD is set to $C_T = 0.65$ to match the experimental measurements of the porous disk (Aubrun et al., 2019). This value is kept constant under platform surge motion. Although the platform motion induces variations in the apparent inflow velocity of approximately $\pm 25\%$ relative to the upstream velocity, the corresponding Reynolds number changes do not significantly affect the aerodynamic drag characteristics of the rigid porous mesh, as previously verified experimentally for varying inflow speeds (Aubrun et al., 2019)[rev].

While this constant C_T approach accurately replicates the passive aerodynamic behaviour of a physical porous disk undergoing surge motion, it introduces a loss of generality when extending the results to a real three-bladed wind turbine rotor. In a physical floating wind turbine, the instantaneous thrust coefficient varies due to changes in tip-speed ratio, pitch control actions, and dynamic inflow effects induced by the platform motion. Consequently, the present AD framework isolates the purely kinematic interaction between the surge motion and the wake dynamics, serving as a fundamental baseline for more complex aeroelastic scenarios.[rev]

2.3 Computational Domain and Boundary Conditions

In the case of laminar and low-turbulence flows, a 25D long domain is built, with a 10Dx10D cross section. This cross-sectional area yields a blockage ratio of less than 1%. Since this value is well below the typical 5% threshold where confinement effects become significant (Sarlak et al., 2016), the numerical domain is wide enough to avoid artificial acceleration around the AD.[rev]

The starting mesh is uniform and various mesh refinements are carried out. In order to capture the surge motion, a higher resolution is required. Therefore, the cells near the AD are twice as large in the cross directions as they are in the flow direction. To carry out a mesh convergence study, four meshes are built under these conditions and compared for the case of a motionless

Table 1. Details about the meshes analysed during the mesh convergence study for laminar flow.

Mesh number	Cells	Cells/D in cross direction	Cells/D in flow direction
1	0.74M	8.8	17.6
2	1.95M	12.8	25.6
3	2.86M	17.6	35.2
4	7.81M	25.6	51.2

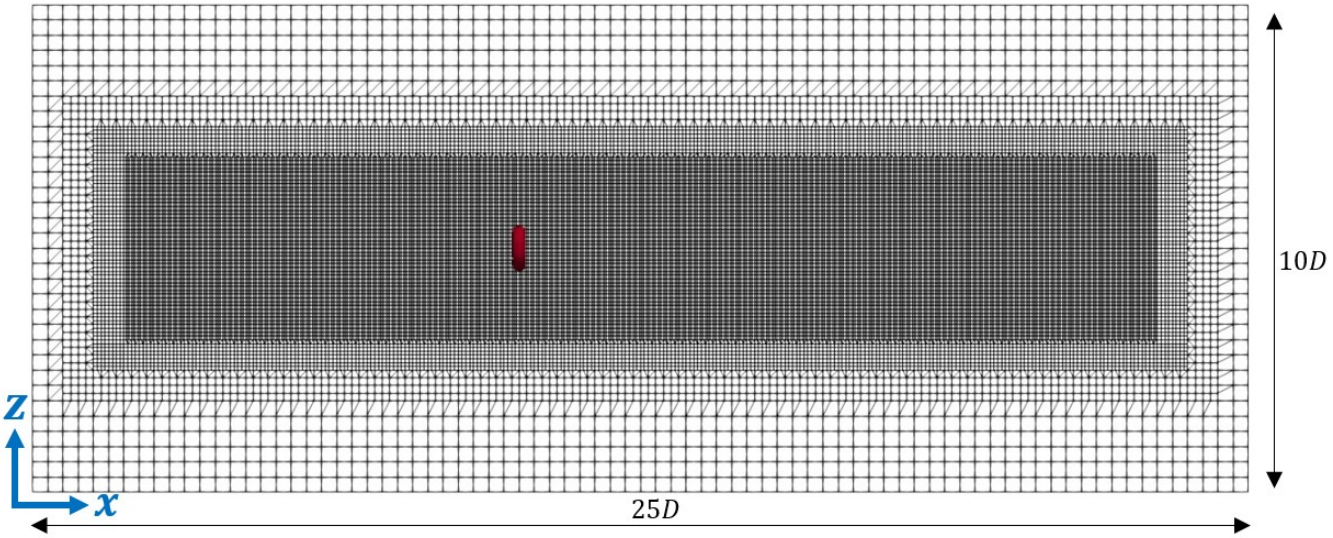

Figure 1. Schematic of the mesh implemented for laminar and low-turbulence flow cases. 8D and 12D are left upstream and downstream, respectively, with the smallest cells.

AD under laminar flow, analysing the wake at 4D, 6D and 8D downstream the AD. The characteristics of the four meshes are presented in table 1 and mesh #2 is shown in Fig. 1. This mesh contains 12.8 cells/D in the cross direction and 25.6 cells/D in the flow direction, and is the one selected for the rest of the study, as will be shown in section 3. Also, the chosen mesh leaves 8D upstream the AD inside the more refined mesh in order to give the flow enough space to develop correctly before arriving at the AD. Finally, 12D are left behind with the same cell size to cover the wake from 2D till 10D.

To achieve a converged ABL flow, many authors have opted for the precursor technique, where the flow is developed by recirculation until convergence, and only then it is presented with the wind farm (Churchfield et al., 2012a, b; Stevens et al., 2014; Lanzilao and Meyers, 2023). In this work, the authors choose to include the precursor region within the simulation domain, as it is done by Chen et al. (2022), and the inlet is set by mapping the end of the precursor region. The zone of analysis is located downstream this region. A schematic of the numerical domain is shown in Fig. 2, where the flow at 75D from the inlet is mapped into the domain inlet Boundary Condition (BC).[rev] For the ABL case, the domain dimensions are 175D long and

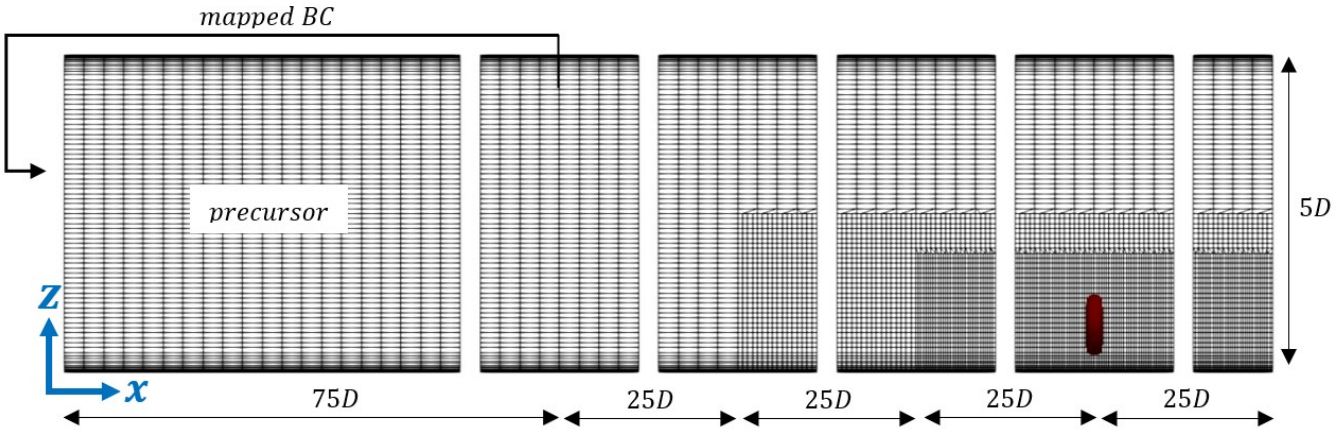

Figure 2. Schematic of the mesh implemented for ABL flow. After the precursor region, 2 mesh refinements are carried out in the horizontal direction.

10D wide, but the height is reduced to 5D. This cross-section yields a blockage ratio of approximately 1.5%, which, similarly to the uniform flow cases, is well below the 5% threshold, ensuring that confinement effects remain negligible. The decision to restrict the domain height is intrinsically linked to the numerical modelling of the Atmospheric Surface Layer (ASL). At real scale, the ASL refers to the lowest portion of the ABL where turbulent quantities and fluxes display a near-constant behaviour (Richards and Hoxey, 1993; Stull, 2012; van der Laan et al., 2020, 2021). Simulating a deep domain for a neutrally stratified ABL without resolving temperature gradients, and thus lacking an inversion capping layer, can lead to an artificial decay of turbulence in the upper portion of the domain. To avoid this issue in the present scaled configuration, the domain height is limited to $5D$. This reduced height is combined with a top stress boundary condition, which provides the required forcing to maintain realistic turbulence levels and preserve a consistent ASL profile over the downstream distance considered (Zahn and Bou-Zeid, 2024).~~The domain dimensions are 175D long, 10D width and 5D height.~~[rev] The mesh contains originally 12.8 cells/D in the vertical direction and 3.2 cells/D in horizontal direction. Also, a mesh height gradient is imposed near the bottom in order to correctly model the flow near the surface, and the same gradient is applied near the top. After the precursor region, based on the previously mentioned mesh convergence study, 2 mesh refinements are carried out only in the horizontal direction, reaching 25.6 cells/D in the region near the AD for both horizontal directions, and 12.8 cells/D in the vertical direction. This mesh refinement continues up to 25D downstream the AD. The resulting total number of cells is 4.84M.

Cyclic lateral BCs are imposed in all cases. For the laminar and low-turbulence cases, the other two boundaries (top and bottom) are set to slip. For the ABL case, stress boundary conditions are prescribed at both faces to sustain the neutral ASL. The bottom boundary follows Schumann's model (Schumann, 1975) to account for the physical surface roughness of the wind tunnel floor, while the top boundary applies a shear-stress condition based on the target friction velocity u^*, similar to what is done by Jimenez et al. (2007), and Zahn and Bou-Zeid (2024).[rev] The inlet boundary condition is set to a velocity fixed value without any perturbation in the laminar case, while a filtered noise boundary condition is applied for the low-turbulence

Table 2. Surge frequency of the cases analysed in this work with the corresponding Strouhal number. In all cases, the amplitude is set to $\frac{D}{8}$.

$f_{surge}[Hz]$	$S_t = \frac{f_{surge}\ D}{U_{ref}}$ rev
0	0
2	0.12
3	0.18
4	0.24
5	0.30
5.5	0.32
6	0.35
8	0.47

case. This type of inflow, as originally proposed by Klein et al. (2003), consists of imposing the desired length scales on a random Gaussian white noise through a filtering operation, and subsequently scaling to achieve the desired Reynolds Stress Tensor. Following this, the targeted mean flow is superimposed on the signal. For the low-turbulence case, the targeted mean flow is entirely uniform (i.e., it contains no vertical shear), and only the turbulent fluctuations are superimposed.[rev] For further details regarding this process, please refer to Immer (2016). The turbulent length scales used for the filtering process in the inlet flow[rev] are set equal to ~~taking into consideration~~[rev] the values obtained[rev] in the ABL flow, but the same length scale is set in~~considering equal length scales in~~[rev] both cross directions. In order to achieve an average uniform flow with a lower turbulence, the same values are specified in the entire inlet surface. Regarding the physical characteristics of the chosen ABL, it is modelled to represent the scaled wind tunnel boundary layer experimentally studied by Schliffke et al. (2024), rather than a specific physical site. Accordingly, the target velocity and turbulence intensity profiles were configured following VDI guideline 3783 (VDI, 2000) for atmospheric boundary layer wind tunnel modelling. This provides a standardised, strongly sheared, and highly turbulent baseline to contrast with the uniform inflow cases without shear.[rev]

2.4 Cases Analysed

Table 2 summarizes the cases analysed in this work. The reference velocity $U_{ref} = 2.71m/s$ is taken at the inlet for the uniform flow cases, and at the AD original position in a simulation without AD for the ABL case. The specific test cases are selected following those in Schliffke et al. (2020, 2024), whose experimental setup was originally designed to replicate the Floatgen project, featuring a 2 MW Vestas V80 wind turbine with a 60 m hub height and an 80 m rotor diameter.[rev]

Although these initial experiments were scaled based on a 2 MW turbine, the selected Strouhal numbers hold direct physical relevance to modern 10 to 15 MW floating wind turbines. For such full scale turbines, characterised by rotor diameters of 180 m to 240 m and near rated wind speeds of approximately 10 to 11 m/s (Bak et al., 2013; Gaertner et al., 2020), the S_t range of 0.12 to 0.47 corresponds to physical oscillation frequencies between 0.005 Hz and 0.03 Hz. This frequency range is representative of the rigid-body platform motions typically observed in spar and semisubmersible floating wind turbines, whose natural

frequencies generally lie between approximately 0.005 Hz and 0.05 Hz for large-scale systems (Allen et al., 2020; Fontanella et al., 2022a). Specifically, a motion amplitude of $\frac{D}{8}$ represents a bounding scenario for extreme resonant responses in these large structures. Consequently, this study focuses strictly on these low-frequency, large-amplitude dynamics, whereas higher reduced frequencies ($S_t > 0.5$), typically associated with first order wave excitation, fall outside the current scope.[rev]

3 Mesh sensitivity analysis and wake flow characterisation~~Preliminary LES Results~~[rev]

This section presents the preliminary results of the LES. First, a mesh convergence study is performed for the laminar inflow case to evaluate the accuracy of the numerical setup. Then, an independent assessment is carried out for the low-turbulence and ABL inflow cases, where the inflow generation method is validated against experimental inflow conditions for the latter. Finally, the vortex ring structure is analysed by examining the vorticity field and the Q-criterion for one of the surge frequencies considered in this work.

In order to verify the mesh convergence, a laminar uniform flow inlet is applied to the four meshes described in Table 1, including the AD with no movement. The first 10s are left for the flow to develop, after which the results of the following 40s are averaged. Based on the time scaling factor of 150 associated with this experimental setup (Schliffke et al., 2024), these intervals translate to approximately 25 minutes of initialization and 100 minutes of continuous data collection at full scale.[rev] The time-averaged velocity deficit profiles of all cases at 4D, 6D and 8D downstream the AD are compared in Figs. 3a, 3b and 3c, respectively.~~The mean flow velocity profiles of all cases at 4D downstream the AD are compared in Fig. 3~~[rev]. It can be seen that mesh #2 already reaches convergence near the wake centre for the flow downstream the AD. This agreement with the finer meshes is maintained at 6D and 8D, where the profiles for mesh #2 show a consistent behaviour across the entire wake width, suggesting that the spatial resolution is adequate for the purposes of this study.[rev]

With regard to the low-turbulence inflow conditions, following mesh refinement, 10s are allowed for the flow to develop in a simulation without the AD. Thereafter, two consecutive 40s periods are run. Figure 4a presents the averaged velocity zoomed around the AD region during the second period, followed by the TI split into three components, in Figs. 4b, 4c and 4d. The initial plot displays a uniform inflow, while the subsequent three plots demonstrate statistical convergence of the flow during these specified periods. In such conditions, a turbulence intensity of approximately 1.2% is obtained, and the integral length scale is found to be approximately $L_u^x \approx 910$ mm.

In order to verify that the ABL wind tunnel profile is accurately reproduced during the simulations, an initial precursor[rev] stage ~~of the simulation~~[rev] is run for 1200s on a base mesh[rev] without mesh refinement or AD. Using the resulting flow field as the initial condition~~Then~~[rev], the two mesh refinements detailed in the previous section are carried out. The simulation is run for an additional 100s (up to t = 1300s)~~after which the simulation is run for a further 100s~~[rev] to allow the flow to develop correctly before the results are recorded. A total of 80s is then run, split into two runs of 40s each. Based on the time scaling factor of 150 (Schliffke et al., 2024), these intervals correspond to 250 minutes of initialization and 100 minutes per run at full scale.[rev] The results for the average velocity, zoomed in the AD region, after 80s are shown in Fig. 5a along with the profile reported in Schliffke et al. (2024), which corresponds to a scaled maritime boundary layer, showing a high degree

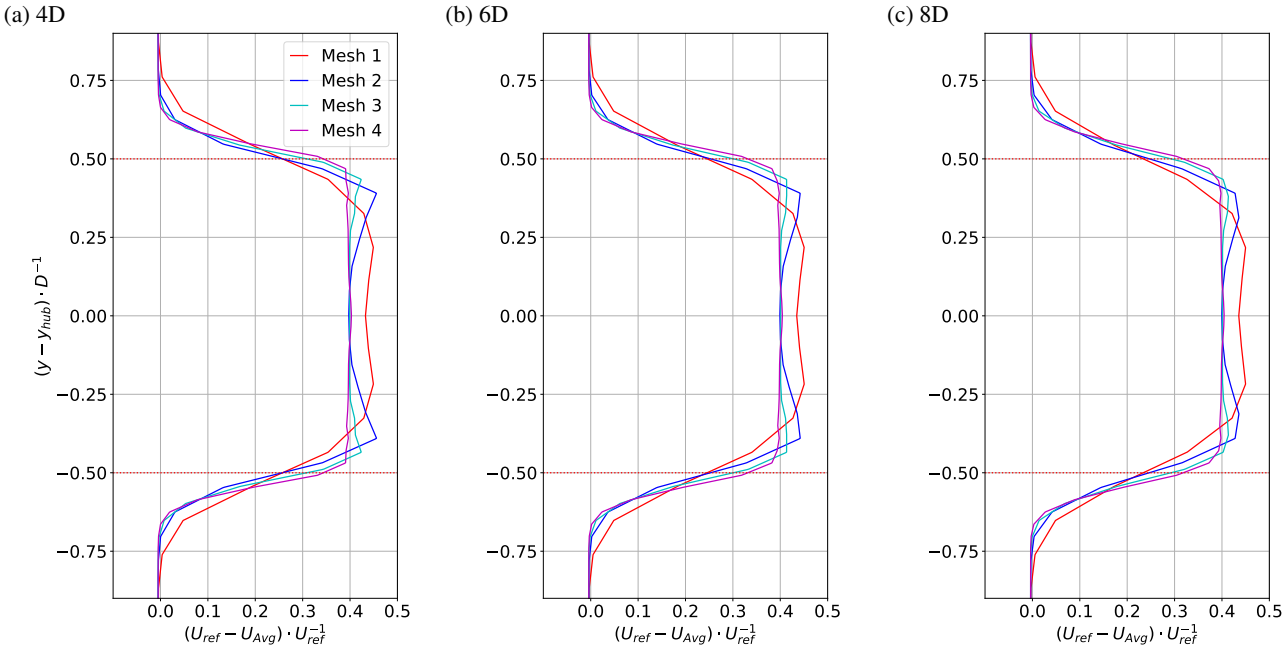

Figure 3. Average velocity deficit results for the mesh convergence study under laminar uniform flow at 4D, 6D and 8D downstream the AD.

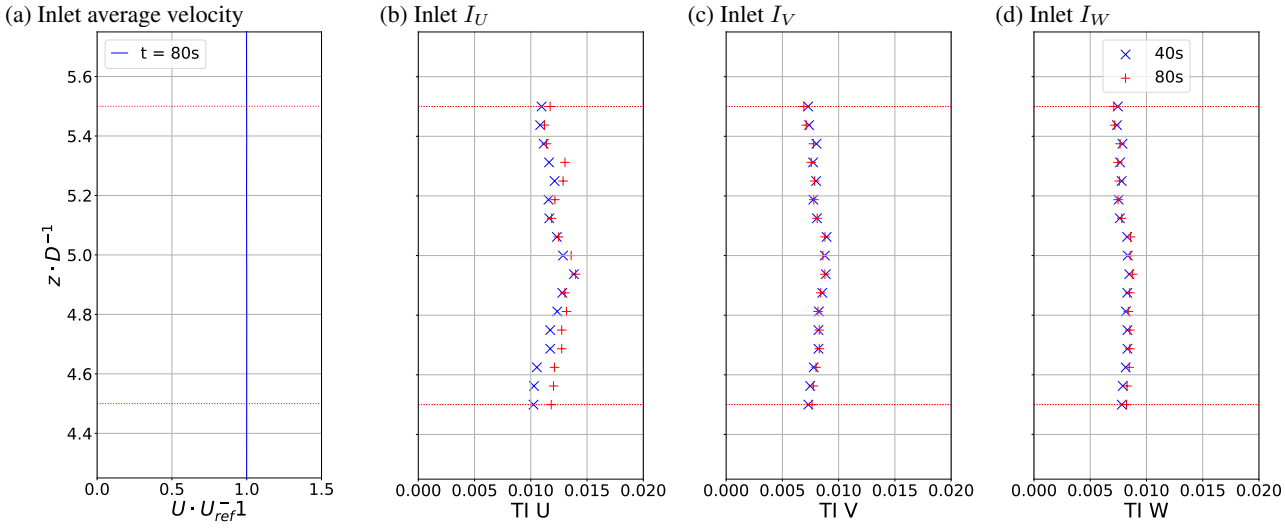

Figure 4. Inlet flow average velocity (a) and TI profiles for the three velocity components (b, c and d) after mesh refinement for low-turbulence flow. All profiles are zoomed in the refined region. The~~the~~[rev] dotted red lines delimit the height of the porous disk.

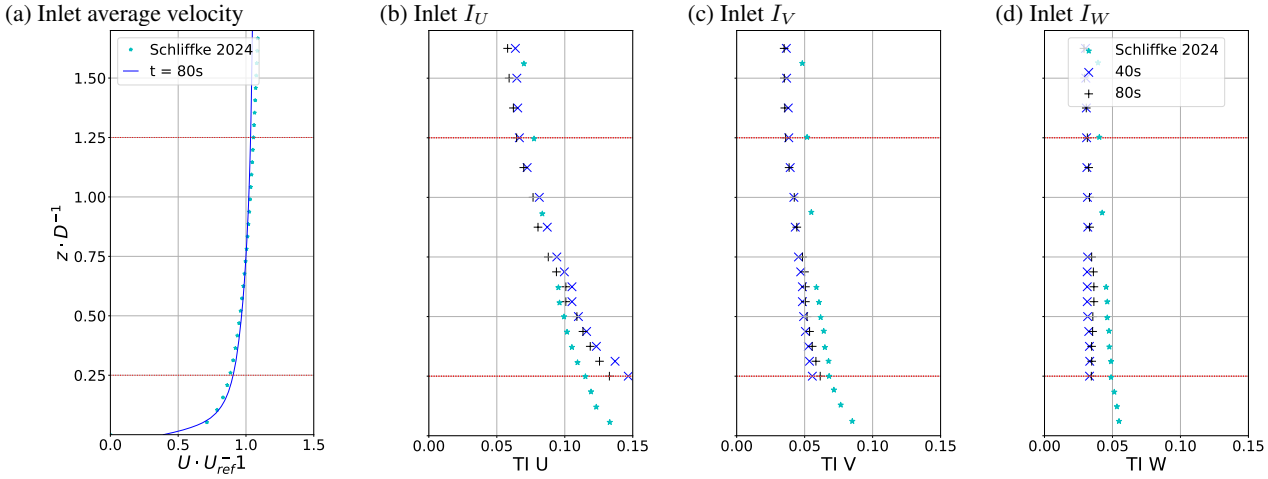

Figure 5. Inlet flow average velocity (a) and TI profiles for the three velocity components (b, c and d) after mesh refinement. All profiles are zoomed in the refined region and compared with experimental values from Schliffke et al. (2024). The dotted red lines delimit the height of the porous disk.

of correlation. Also, each component of the turbulence intensity for the two 40s run is shown in Figs. 5b, 5c and 5d, which demonstrate statistical convergence between the two periods. The experimental values reported in Schliffke et al. (2024) are also included for comparison.[rev] When comparing with these~~the~~[rev] experimental values, the CFD exhibits a close match across all three components, with a slight surplus observed in the U component and a slight deficit in V and W components. In such conditions, a turbulence intensity of approximately 9% is obtained at hub height, and the integral length scale at this point is found to be approximately $L_u^x \approx 750$ mm, which is of the same order of magnitude as the experimental value reported in Schliffke et al. (2024); Hubert et al. (2025), $L_u^x \approx 480$ mm. For the cases including the AD, the process is repeated, starting with the results of the first 1200s. The AD is activated when the mesh refinements are carried out, and 100s are left for the wake to develop.

For the three inflow conditions (laminar, low-turbulence and ABL), the cases from table 2 are simulated as described. Data recording starts at 10s for the laminar and low-turbulence inflow cases, and at 1300s for the ABL inflow case. Two consecutive simulation periods of 40s each are performed with the moving AD. In a first attempt to visualise the flow structure, Q-criterion contours ($Q = 50$) are presented for a harmonic surge motion at $S_t = 0.32$ under laminar, low-turbulence and ABL flows in Figs. 6a, 6b and 6c, respectively. The figure clearly shows the vortex ring structure for both the laminar and low-turbulence inflow cases. This vortex ring structure was previously visualised under uniform inflow for a variety of S_t values: Arabgolarcheh et al. (2023b) for $S_t = 0.08$ and 0.18, Duan et al. (2022) and Zhou et al. (2025) for $S_t = 0.55$, Wang et al. (2024) for $S_t = 0.69$ and Arabgolarcheh et al. (2023a) for $S_t = 1.22$. In contrast, the ABL flow exhibits no clear structure in the wake. This was also the finding of Xu et al. (2024), in which the vortex structure was clear for uniform and shear inflows, but there was no visible pattern in the wake under turbulent ABL conditions. The same situation arises for the other movement

(a) Q – Laminar inflow

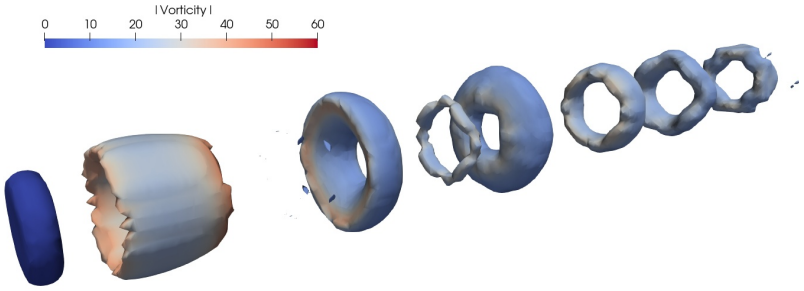

(b) Q – Low-turbulence inflow

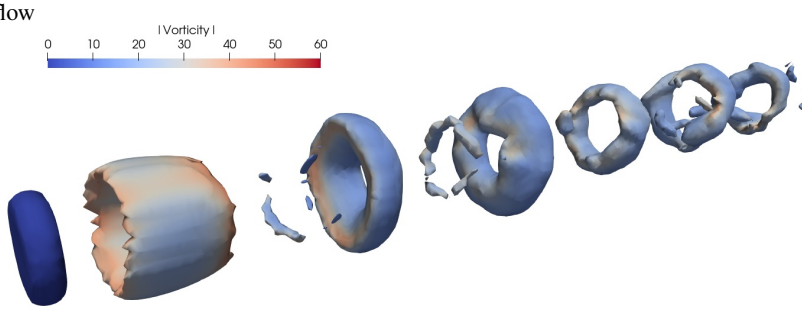

(c) Q – ABL inflow

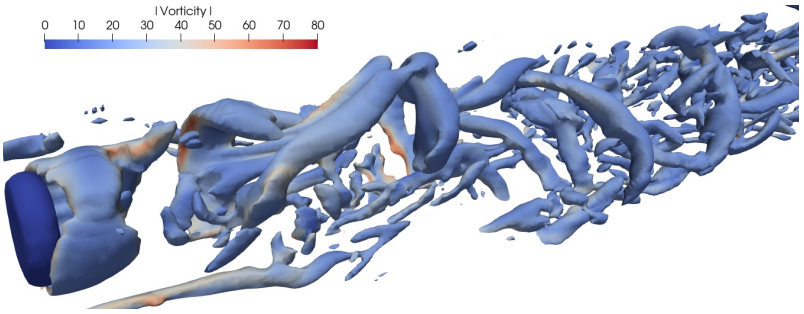

Figure 6. Q-criterion contours ($Q = 50$) for $S_t = 0.32$ under laminar (a), low-turbulence (b) and ABL (c) inflows. The contours are coloured by vorticity magnitude.

frequencies. In order to gain a clearer understanding of the structures involved, POD will be applied to these results in the following section.

4 Proper Orthogonal Decomposition

The POD is a statistical technique originally developed by Lumley (1967) to extract the most energetic coherent structures from turbulent flows by projecting data onto an optimal orthogonal basis. Later, Sirovich (1987) reformulated it into the so-called snapshot method, which made the approach computationally efficient for large datasets. The resulting modes are presented sorted by energy content. The following steps are taken when applying the POD technique in this work. During the last 40s of

each CFD run, once the flow has reached a[rev] converged statistics, snapshots of the wake are taken in a vertical plane parallel to the AD axis at a sampling frequency of 100 Hz. Data is extracted from 2D downstream of the AD to 10D, considering only streamwise and vertical velocity components. POD is applied to these results using the MODULO software (Ninni and Mendez, 2020), which implements Sirovich's snapshot method. The result is a decomposition in the form:

$$u'(\mathbf{x},t) = \sum_{P=1}^{N} \sigma_P \Phi_P(\mathbf{x}) \Psi_P(t), \tag{5}$$

where Φ_P and Ψ_P are the spatial and temporal modes respectively sorted by energy content, and σ_P is the square root of the energy of the associated mode. Physically, the spatial modes (Φ_P) represent the most energetic coherent spatial structures of the flow, while the temporal modes (Ψ_P) describe the temporal evolution of the projection of the flow onto each spatial mode.[rev] $u'(\mathbf{x},t)$ corresponds to the in-plane velocity fluctuations as the mean velocity is subtracted before computing the POD.

In this work, POD spatial modes are used to reveal flow structures that could not be identified using the Q-criterion in section 3, and POD temporal modes to discriminate whether the associated flow structures are correlated with the imposed harmonic movement. The latter is done by computing the Fourier transform of the temporal modes. In all cases, the technique is applied to the velocity fluctuations in the plane $X-Z$ between 2D and 10D downstream the AD. A total of 3600 modes are calculated for each case, and 90% of accumulated energy is achieved, depending on the frequency, within approximately 10 modes for laminar inflow, 30 modes for low-turbulence inflow and 100 modes for the ABL inflow.

4.1 POD - Laminar

The laminar inflow case is considered in the initial stage in order to establish a reference for the subsequent cases. Figure 7 shows the energy content for each mode, which is obtained as the square of the singular value corresponding to the mode in equation 5, normalized by the total of this quantity. Results are shown for $S_t = 0$, $S_t = 0.24$ and $S_t = 0.32$, in Figs. 7a, 7b and 7c, respectively. These frequencies are representative of all the cases observed (see Table~~table~~[rev] 2). In all figures, the most energetic modes include pairs with similar energy content. Particularly for the cases with surge motion ($S_t = 0.24$ and $S_t = 0.32$), this pairing provides a clear baseline to understand how POD captures flow dynamics. In the context of POD, this *mode pairing* is the mathematical signature of a travelling wave or a convecting coherent structure, such as the vortex rings generated by the AD surge motion. Because these structures continuously change their downstream position over time, a single stationary spatial mode is insufficient to describe them. Consequently, the POD algorithm decomposes this advection into a pair of orthogonal spatial modes that exhibit similar spatial patterns but present a $\pi/2$ phase shift in the streamwise direction. When these paired spatial modes are multiplied by their corresponding harmonic temporal modes, which oscillate at the same frequency but are also phase-shifted in time, their linear combination accurately reconstructs the continuous downstream advection of the vortices. Following this interpretation,[rev] Figs. 8a, 8b and 8c show the first four spatial modes for $S_t = 0$, $S_t = 0.24$ and $S_t = 0.32$, respectively. The resulting modes are displayed using vectors indicating the direction of the local velocity fluctuation, and are coloured by the fluctuation magnitude, normalized by the maximum value in each case. It is evident that all three cases confirm the presence of pairs of opposite modes (1 and 2, 3 and 4). Also, all modes displayed in

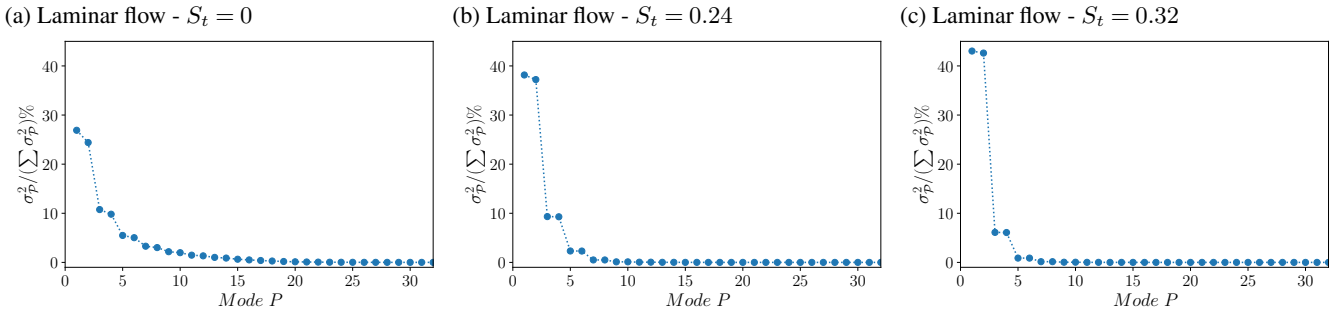

Figure 7. Energy distribution across modes for $S_t = 0$ (a), $S_t = 0.24$ (b) and $S_t = 0.32$ (c), under laminar flow.

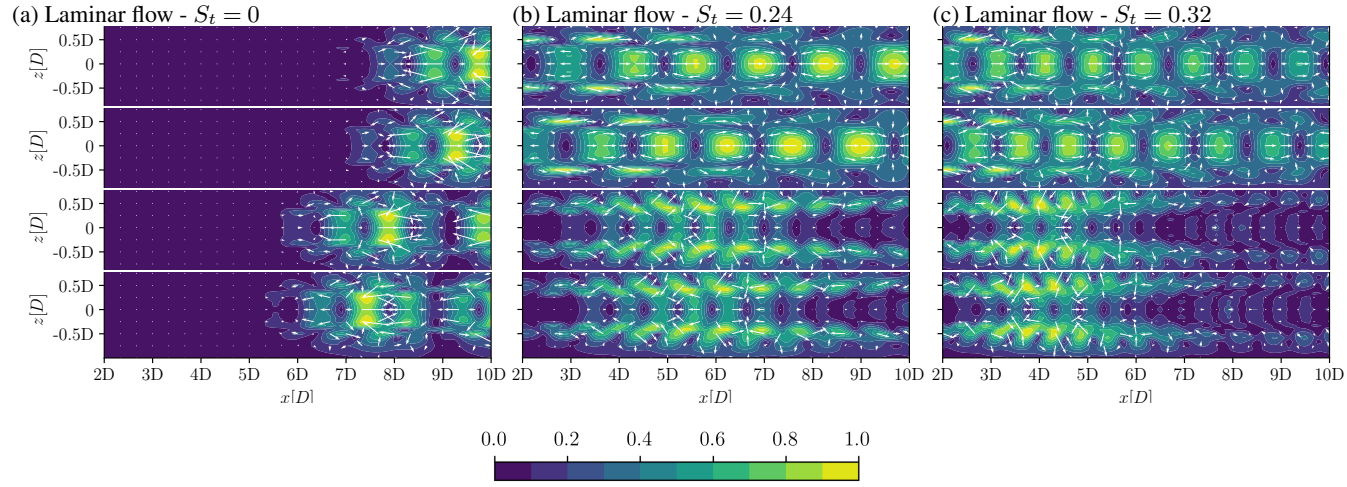

Figure 8. First four spatial modes $\Phi_1(\mathbf{x}) - \Phi_4(\mathbf{x})$ resulting from POD analysis applied to surge cases with $S_t = 0$ (a), $S_t = 0.24$ (b) and $S_t = 0.32$ (c), under laminar flow. The modes are displayed with vectors indicating the direction of the local velocity fluctuation, and are coloured by the fluctuation magnitude, normalized by the maximum value in each case.

pairs present the same Fourier spectrum of the time component (not shown here), thus confirming that they belong to the same vortex structure. The frequencies present in modes 1 and 3 for each case are shown in Figs. 9a, 9b and 9c.

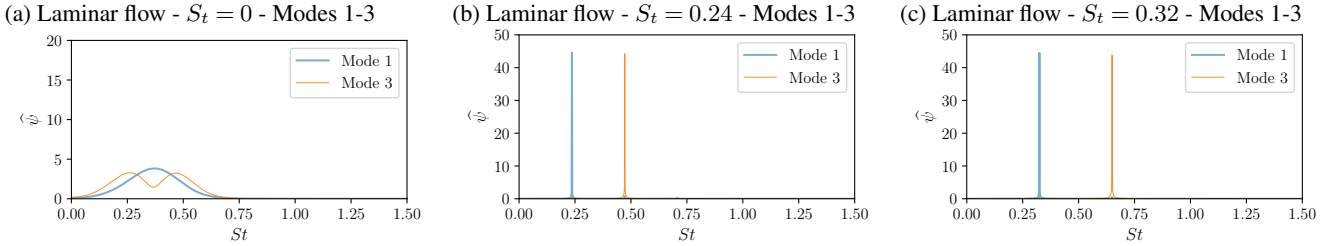

Figure 9. Fourier spectrum of the temporal modes $\Psi_1(t)$ and $\Psi_3(t)$ for $S_t = 0$ (a), $S_t = 0.24$ (b) and $S_t = 0.32$ (c), under laminar flow.

In the absence of motion, that is, when $S_t = 0$, the spatial modes are found to be symmetric with respect to the AD axis ($z = 0$ in Fig. 8a). This observation indicates that the situation is not one of alternating vortex shedding. Furthermore, the frequencies exhibited in the modes, as illustrated in Fig. 9a, show a distributed energy content across a specific band of frequencies ($S_t \approx 0.2 - 0.55$). While a broadband frequency distribution could theoretically indicate the presence of physical mechanisms whose exact frequency and lateral expansion slowly evolve over time (such as wake meandering), the spatial modes here remain strictly symmetric (Fig. 8a), contradicting an alternating meandering behaviour. Instead, these modes most likely correspond to the advection of negligible residual fluctuations in the wake, as the maximum velocity magnitude reconstructed from them is six orders of magnitude smaller than the mean velocity field. This confirms the absence of any dominant coherent structure under stationary laminar conditions.[rev]

On the other hand, besides presenting the energy content in pairs (Figs. 7b and 7c), cases $S_t = 0.24$ and $S_t = 0.32$ exhibit a discernible pattern for spatial modes 1 and 2, associated with the advection of the vortex ring structure visualised in section 3 (Figs. 8b and 8c). In addition, modes 3 and 4 correspond to the first harmonic of this configuration, as illustrated by their spectra in Figs. 9b and 9c. Also, both pairs of modes present symmetry with respect to the AD axis ($z = 0$) in terms of velocity direction. For modes 1 and 2, the only prevailing frequency is the surge frequency, whereas for modes 3 and 4, it is the double of this frequency. It is noticeable that $S_t = 0.32$ exhibits higher energy in the first pair of modes and lower energy~~a minor~~[rev] in the harmonics, compared to $S_t = 0.24$. In both cases approximately 94% of the total energy is contained within the first four modes, which is consistent with the findings of Wang et al. (2024), where these modes accounted for about 95% of the total energy under uniform flow. It is worth mentioning that modes 5 to 10, not shown in this work, behave in a similar way, displaying pairs of different harmonics of the vortex ring structure. Also, in all cases analysed, more than 99.9% of the energy is accumulated within the first ten modes, showing that there is no other strong coherent structure present. These observations suggest that the vortex ring structure is a prevailing feature under laminar flow within the specified frequency range. Furthermore, it agrees with the observations made in previous studies, which reported the visualisation of the vortex ring structure for a broad range of frequencies, ranging from $S_t = 0.08$ to $S_t = 1.22$, under uniform inflow conditions, as discussed in section 3. In addition, a visual inspection of the spatial modes in Fig. 8 reveals that the coherent pulsation associated with the first pair of modes maintains its structural integrity as it is convected downstream. This persistent coherence is a direct consequence of the complete absence of background turbulence, allowing the structures generated by the surge motion to evolve without external disruption.[rev]

4.2 POD - Turbulent

The analysis continues with the application of POD to the low-turbulence flow results, with the objective of investigating how the behaviour changes in the presence of turbulence. The energy content for each mode is presented in Figs. 10a, 10b, 10c for the cases of $S_t = 0$, $S_t = 0.24$ and $S_t = 0.32$, respectively. These results are followed by the first six spatial modes for each case in Figs. 11a, 11b and 11c. In contrast with the laminar no-motion case, where mode pairing was exhibited, the $S_t = 0$ case presents six distinctly different energy contents for the first six modes characterised by a linear decay (Fig. 10a). Also, the spatial modes in Fig. 11a show asymmetry in terms of velocity direction, as evidenced by the arrows above and below

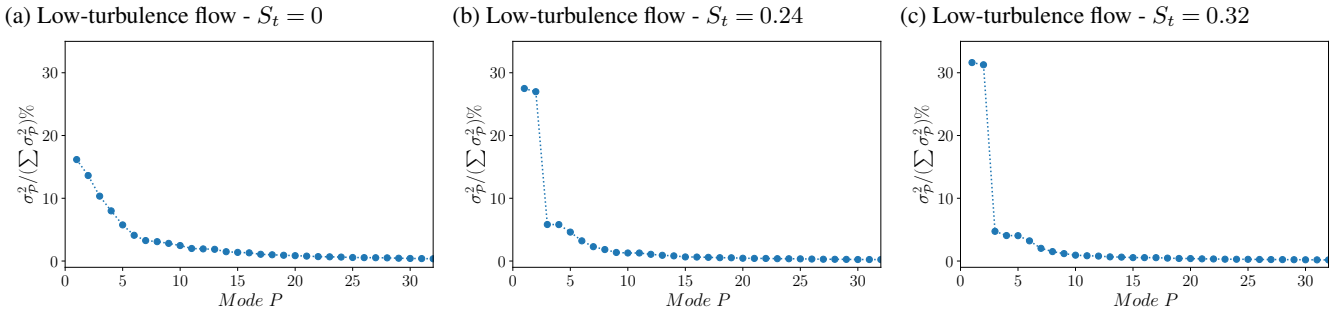

Figure 10. Energy distribution across modes for $S_t = 0$ (a), $S_t = 0.24$ (b) and $S_t = 0.32$ (c), under low-turbulence flow.

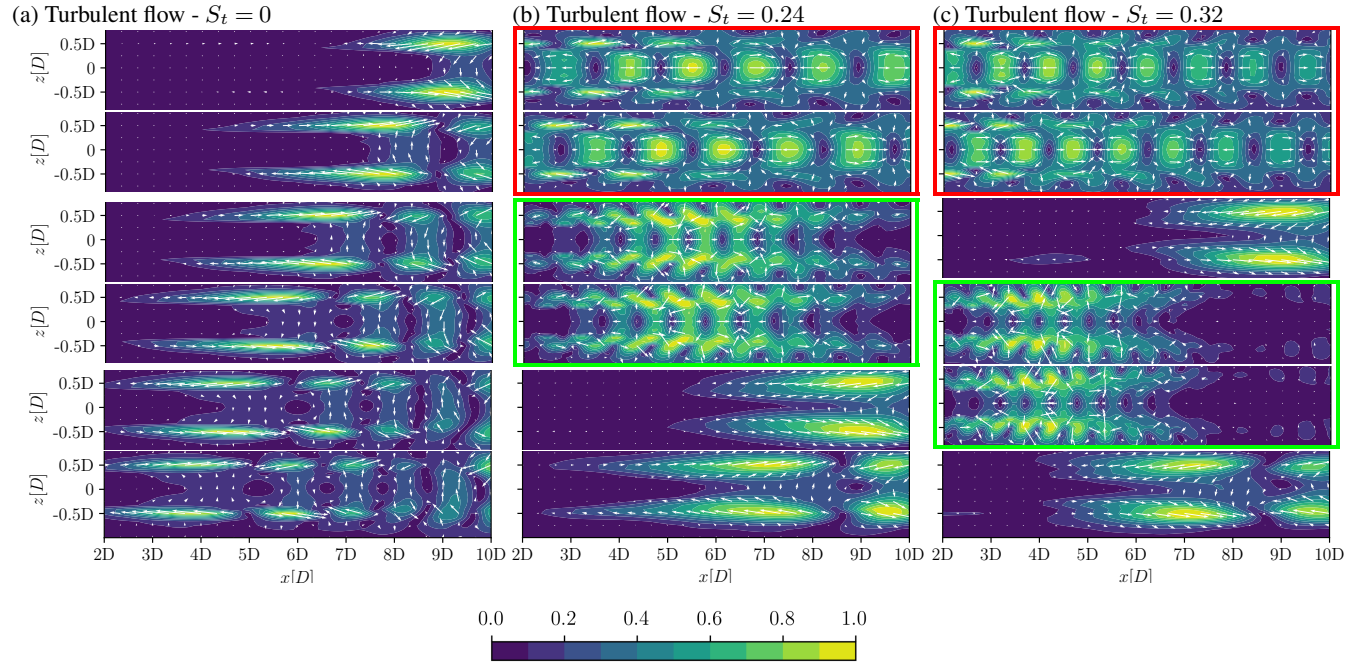

Figure 11. First 6 spatial modes $\Phi_1(\mathbf{x}) - \Phi_6(\mathbf{x})$ resulting from POD analysis applied to cases with $S_t = 0$ (a), $S_t = 0.24$ (b) and $S_t = 0.32$ (c), under low-turbulence flow. Pairing modes are outlined in red for the case of the main pair (modes 1 and 2 in $S_t = 0.24$ and $S_t = 0.32$), and in green for pairing corresponding to harmonics of f_{surge} (modes 3 and 4 in $S_t = 0.24$ and modes 4 and 5 in $S_t = 0.32$). The modes are displayed with vectors indicating the direction of the local velocity fluctuation, and are coloured by the fluctuation magnitude, normalized by the maximum value in each case.

the AD axis ($z = 0$), which point in directions that are not congruent. This suggests an alternating behaviour, such as vertical meandering. Considering the frequency spectrum of modes 1 and 3 (Fig. 12a), it can be seen that the frequency ranges neither match between modes nor show a harmonic relation. The results obtained indicate the presence of meandering phenomena throughout the wake, which is distributed along six modes. A higher energy allocation is observed in the tail of the wake, due to increased wake movement in that sector.

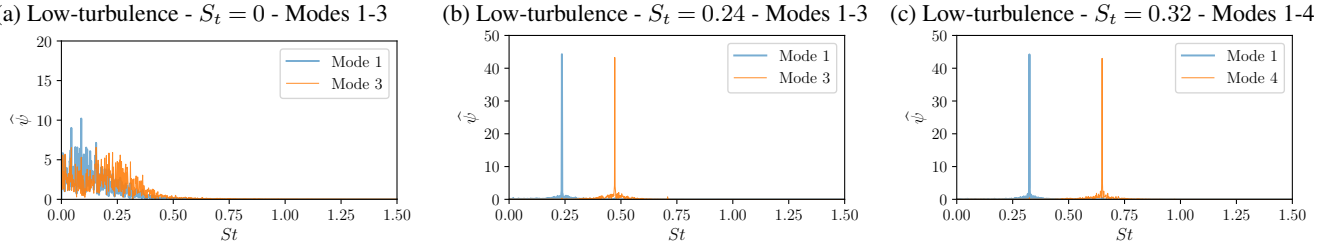

Figure 12. Fourier spectrum of the temporal modes $\Psi_1(t)$ and $\Psi_3(t)$ for $S_t = 0$ (a), $\Psi_1(t)$ and $\Psi_3(t)$ for $S_t = 0.24$ (b) and $\Psi_1(t)$ and $\Psi_4(t)$ for $S_t = 0.32$ (c), under low-turbulence flow.

In the $S_t = 0.24$ case, it can be observed in Fig. 10b that the first two modes show similar energy content, corresponding to a *mode pairing* situation. Modes 3 and 4 show a similar pattern. This is confirmed in Fig. 11b where modes 1 and 2 show pairing corresponding to the vortex ring structure, and modes 3 and 4 show a pattern related to the first harmonic of the same structure. These patterns are symmetric with respect to the AD axis ($z = 0$), as it was the case for laminar flow in Fig. 8b. Furthermore, the Fourier spectra of modes 1 and 3 (Figure 12b) show a single peak corresponding to the surge frequency and twice the surge frequency, respectively. A novel feature is that now, spatial modes 5 and 6 show good agreement with the first two modes in the no motion case. This indicates that, within the most energetic modes, two new modes emerge that are related to the wake meandering rather than the vortex ring structure. The range of frequencies in these modes, not shown here, matches closely~~are a great match~~[rev] with modes 1 and 2 from the $S_t = 0$ case. Also, the energy distribution presented in Fig. 10b shows that these modes are not paired, resembling the behaviour exhibited for $S_t = 0$.

For $S_t = 0.32$, a similar situation is evident for modes 1 and 2, where a clear mode pairing can be seen in Figs. 10c and 11c. This corresponds to the vortex structure shown in Fig. 6b. However, instead of the second harmonic, the spatial mode 3 resembles the first mode corresponding to the no-motion case. This means the second harmonic signature is slightly less energetic than for the previous motion frequency, as the corresponding modes fall behind the wake meandering mode. The second mode pairing related to double the surge frequency appears in modes 4 and 5. Finally, mode 6 shows the second mode corresponding to the no-motion case, that is, mode 2 for $S_t = 0$. In addition, the frequency spectra of modes 1 and 4 displayed in Fig. 12c agree with these observations.

To summarize the results of the POD analysis of the eight cases in Table 2, Fig. 13a and 13b show the energy content of the first 10 modes for each case. The filled markers connected by a line indicate mode pairing corresponding to the surge frequency, while harmonics are connected with dotted lines. The mode pairing is clear in all cases, where the modes have a similar energy and frequency spectrum. However, the harmonics in St = 0.18 present an arrangement of three modes. In addition, a local maximum is exhibited by the energy content of the pairing modes. This is more clearly seen in Fig. 13c, where the combined energy in both modes and harmonics corresponding to the vortex structure is shown against the S_t number. The total energy captured by the vortex ring structure for the laminar cases has been added to Fig. 13c for comparison. In the laminar regime, the absence of background turbulence makes the structures generated by the surge motion accumulate nearly 100% of the kinetic energy across all frequencies. Conversely, under inflow conditions with low turbulence, the energy

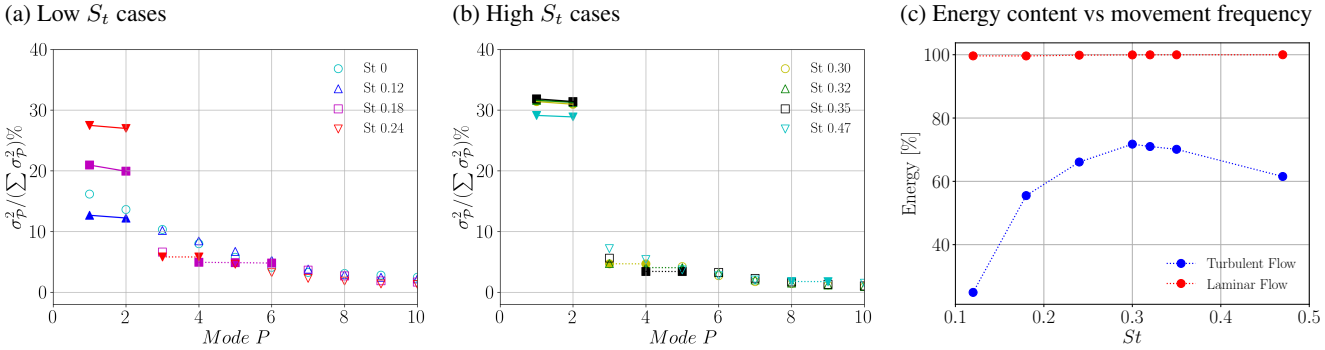

Figure 13. Energy content per mode in Low and High S_t values (a and b) and corresponding to the combined contribution of all modes associated with the vortex ring structure (c) as a function of the S_t number, under low-turbulence flow. In the first two plots, the filled markers connected by a dashed line indicate mode pairing corresponding to the surge frequency, while harmonics are connected with dotted lines.

allocation drops significantly. It is apparent that for the turbulent case at $S_t = 0.30$, the structure attains its maximum relative energy and subsequently begins a decline as the movement frequency increases. This direct comparison demonstrates that the presence of background turbulence, along with induced phenomena such as wake meandering, severely limits the energy that the vortex rings can retain. Furthermore, contrasting the spatial modes from both regimes (Figs. 8 and 11) reveals that, while the coherent pulsation in the laminar case maintains its amplitude as it convects downstream (first two modes in Fig. 8b), the equivalent structures in the turbulent cases visibly start dissipating in the far wake region. This confirms that even a low level of background turbulence is sufficient to trigger the disruption of the pulsating structures. Ultimately, these results indicate that a characteristic frequency of approximately $S_t = 0.30$ appears to be the most stable for the propagation of the vortex ring structure under the evaluated conditions with low turbulence.[rev]

4.3 POD - ABL

In the case of ABL flow, the results differ significantly from those of the previous cases. In Figs. 14a, 14b and 14c the energy content for each mode is displayed for the cases of $S_t = 0$, $S_t = 0.24$ and $S_t = 0.32$, respectively, followed by the corresponding first six spatial modes in Figs. 15a, 15b and 15c. In the no-motion case, the two most energetic modes exhibit an uneven distribution of energy, with the first mode having a markedly higher energy content than the second (Fig. 14a). Also, these two modes exhibit a new spatial distribution (Fig.15a), and a frequency spectrum that spans lower frequencies (Fig. 16a). Instead of a mode pairing~~paring~~[rev] situation, the modes can be associated with the inlet ABL flow and its interaction with the AD. Subsequently, modes 3 to 6 manifest distinctive characteristics analogous to those observed in the no-motion case under low-turbulence flow, that is, a quasi-linear behaviour in the energy content decay and a non-symmetric behaviour in terms of velocity direction, as evidenced by the arrows in Fig. 15a. Then, these modes can also be associated with a wake meandering phenomenon divided in four modes, where the energy content is once again higher at the tail of the wake due to a stronger oscillation.

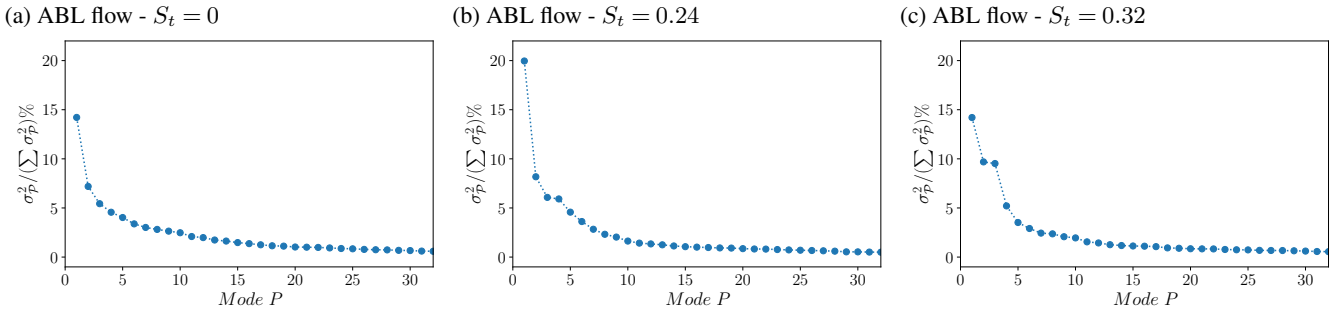

Figure 14. Energy distribution across modes for $S_t = 0$ (a), $S_t = 0.24$ (b) and $S_t = 0.32$ (c), under ABL flow.

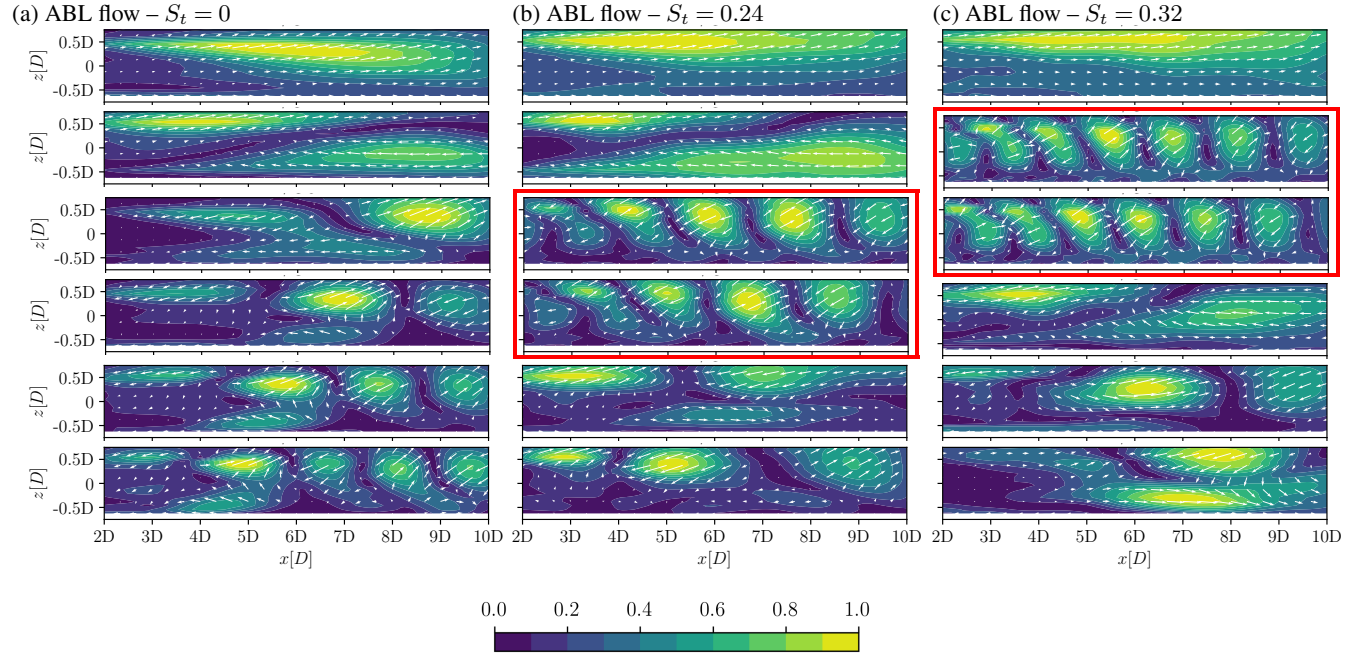

Figure 15. First 6 spatial modes $\Phi_1(\mathbf{x}) - \Phi_6(\mathbf{x})$ resulting from POD analysis applied to cases with $S_t = 0$ (a), $S_t = 0.24$ (b) and $S_t = 0.32$ (c), under ABL flow. Pairing modes are outlined in red (modes 3 and 4 in $S_t = 0.24$ and modes 2 and 3 in $S_t = 0.32$). Modes corresponding to inlet flow and no motion case are the ones resembling modes 1 and 2 in $S_t = 0$ (modes 1 and 2 in $S_t = 0.24$ and modes 1 and 4 in $S_t = 0.32$.)

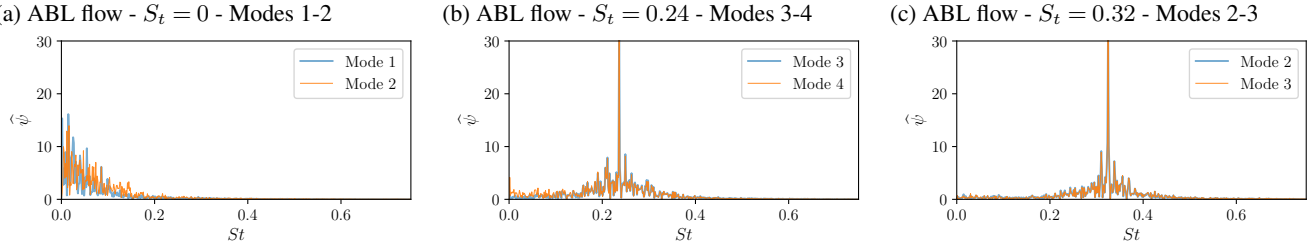

Figure 16. Fourier spectrum of the temporal modes $\Psi_1(t)$ and $\Psi_2(t)$ for $S_t = 0$ (a), modes $\Psi_3(t)$ and $\Psi_4(t)$ for $S_t = 0.24$ (b) and modes $\Psi_2(t)$ and $\Psi_3(t)$ for $S_t = 0.32$ (c), under ABL flow. Modes 1 and 2 for $S_t = 0.24$ and modes 1 and 4 for $S_t = 0.32$ have similar spectra as the ones displayed by modes 1 and 2 in $S_t = 0$.

Regarding the $S_t = 0.24$ case, Fig. 14b exhibits a significantly higher energy in the first mode, in comparison to the other modes, as observed in the no-motion case. The vortex pairing can be identified due to the similarity in energy content between modes 3 and 4. Also, it can be noticed that the spatial modes 1 and 2 in Fig. 15b show a high degree of agreement with the same modes from $S_t = 0$. This similarity is absent in modes 3 and 4, where $S_t = 0.24$ exhibits a pair of opposite modes, as was previously observed in the context of laminar and low-turbulence inflow conditions. Furthermore, the Fourier spectrum of both modes, as illustrated in Fig. 16b, reveals a clear peak at the S_t that corresponds to the surge movement, with no other frequencies observed. Consequently, it can be deduced that the vortex ring structure is present in this case, and that the first two modes are related to the inlet flow and an interaction with the AD similar to that of the no-motion case. Additionally, the Fourier spectrum of these modes, not shown here, exhibit a close match with the ones for modes 1 and 2 in $S_t = 0$. In this instance, the spatial modes corresponding to the vortex ring structure show no symmetry with respect to the AD axis ($z = 0$) in terms of velocity direction, unlike the laminar and low-turbulence cases. This indicates that, under ABL conditions, the vertical meandering and vortex ring structures are strongly coupled, as the surge motion interacts with the ambient shear flow to induce a synchronised, meandering phenomenon.~~This type of spatial mode can be related to a vertical meandering phenomenon taking place specifically due to the combination of surge motion and shear flow.~~[rev] In relation to the remaining two modes depicted in Fig.15b, mode 5 has not been previously observed and is characterised by an absence of a peak related to the surge frequency in its Fourier spectrum (not shown). Finally a certain degree of similarity is observable between mode 6 and mode 4 from the no-motion case, which can also be related to vertical meandering.

The energy content for $S_t = 0.32$, displayed in Fig.14c, shows a single first mode less energetic than for $S_t = 0.24$, followed by a mode pairing between modes 2 and 3. This indicates that the energy associated with this structure is higher at this frequency than at the previous one, thus explaining the notorious reduction in the energy content of the first mode. The energy of the structure was found to vary with the surge frequency for low-turbulence flow, although the vortex pairing shifted to higher modes in this instance. This is corroborated by the spatial modes displayed in Fig.15c where a first mode similar to the previous cases is shown, followed by a mode pairing between modes 2 and 3. Furthermore, the Fourier spectra depicted in Fig. 16c reveals the absence of any other frequency except that corresponding to the movement. This finding suggests that these modes are exclusively associated with the vortex ring structure. Once again, the modes show no symmetry with respect

to the AD axis ($z = 0$) in terms of velocity direction, indicating a vertical meandering phenomenon which is driven by the combination of surge motion and shear flow. Additionally, the spatial mode 4 bears a strong resemblance to mode 2 of the $S_t = 0$ case, indicating that these modes are not associated with the AD motion, but rather with the inlet flow. In a manner analogous to that observed in the $S_t = 0.24$ case, two novel modes emerge which do not contain the motion frequency in their spectra (5 and 6). Nevertheless, these modes demonstrate the impact of the vortex ring structure on wake behaviour.

Figures 17a and 17b show the energy share of the first ten modes for all the cases in Table 2. The filled markers connected by a line indicate mode pairing. Two points merit consideration. On the one hand, the energy associated to modes in the same structure is almost uniform in all cases except for $S_t = 0.12$ and $S_t = 0.18$. In the first one, the surge frequency manifested in other modes but no new mode emerged due to the surge motion. In the second, both pairing modes have additional minor peaks of varying frequencies apart from the movement frequency on their spectrum (not shown here), which may have led to alterations in the energy content. This indicates that the convective structures within this range may not yet have attained sufficient strength, consistent with the threshold of $S_t > 0.19$ reported by Schliffke et al. (2024) for a clear signature at 8D downstream, under ABL flow. On the other hand, a local maximum is exhibited by the energy content of the pairing modes. This phenomenon is more clearly seen in Fig. 17c, where the combined energy of both modes is shown against the S_t number. It is apparent that for the case of $S_t = 0.32$ the structure attains its maximum energy and subsequently begins to decline as the movement frequency increases. When comparing with the low-turbulence case in Fig. 13c, a similar pattern is observed in the energy of the structure, which varies with frequency. In this instance, the peak manifests at $S_t = 0.32$ instead $S_t = 0.30$ and with a marked increase in the energy content, indicating that a characteristic frequency in proximity to this value favours the propagation of the vortex ring structure for the surge motion conditions studied. Furthermore, the decline in the energy content as the frequency increases is more pronounced in the case of the ABL flow. The presence of more turbulent, complex structures appears to have led to a further reduction in the energy present in the vortex ring structure, given that its energy content is much lower than in the low-turbulence case. In addition, Schliffke et al. (2024) also reported that the highest energy levels occur close to $S_t \approx 0.30$ for ABL, which is in agreement with the values obtained in this work. This comprehensive comparison with laminar and low-turbulence inflows has~~have~~[rev] revealed distinct behaviours of the vortex ring structure and the wake in general within the investigated range when ABL flow is considered.

4.4 Analysis of Lateral Wake Meandering

The POD analysis on a vertical plane revealed, among other details, the presence of vertical meandering for the cases under low-turbulence and ABL inflow conditions~~flow~~[rev]. In the low-turbulence scenario, the dynamics of the vortex ring structure and the wake meandering behaved as decoupled phenomena, captured by distinct POD modes with separated frequencies. Furthermore, in neither the temporal modes did the surge frequency appear within the meandering modes. However, under ABL conditions, these phenomena became highly coupled. The POD mode associated strictly with the surge frequency revealed a spatial structure that inherently includes vertical meandering. This indicates that, in a highly turbulent and sheared environment, the surge motion itself acts as an additional mechanism that triggers an induced meandering phase-locked to the platform's oscillation.~~In the first case, the vertical meandering was triggered by the inflow conditions, as the spatial modes were present~~

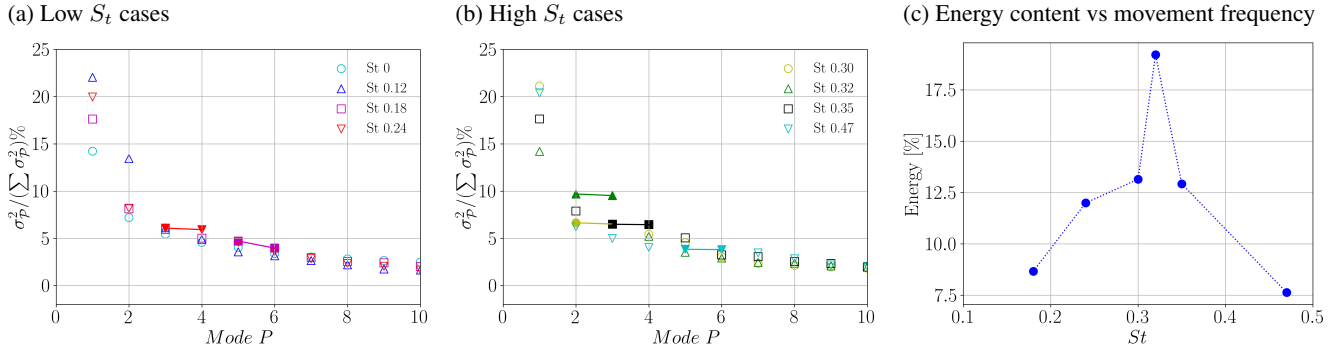

Figure 17. Energy content per mode in Low and High S_t values (a and b) and corresponding to the combined contribution of the two modes associated with the vortex ring structure (c) as a function of the S_t number, under ABL flow. In the first two plots, the filled markers connected by a dashed line indicate mode pairing.

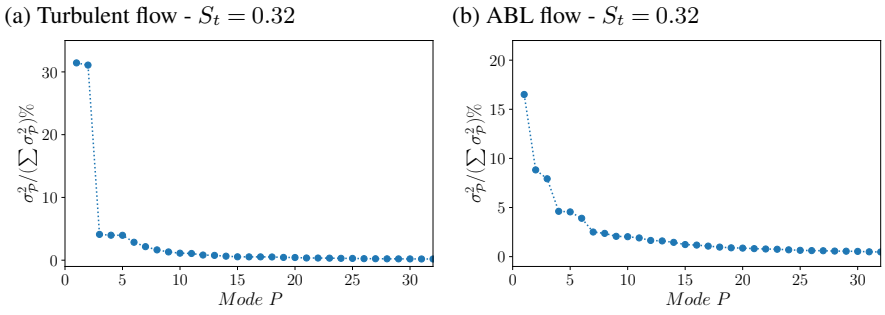

Figure 18. Energy distribution across modes resulting from POD analysis applied to a horizontal plane on cases with $S_t = 0.32$ under low-turbulence flow (a) and ABL flow (b).

~~for both the motion and no-motion cases analysed. Furthermore, in neither the temporal modes did the surge frequency appear within the meandering modes. Conversely, under ABL flow conditions, a pronounced vertical meandering was observed in the modes associated with the vortex ring structure, a phenomenon attributable to the interaction of surge motion and shear flow.~~[rev]

In order to delve deeper into this phenomenon, a similar analysis is carried out in this section but on a horizontal plane, with the intention of identifying side-to-side meandering. The data is obtained in the same periods analysed before, with the same sampling frequency. Considering the moving AD at $S_t = 0.32$, Figs. 18 and 19 show the energy content and spatial modes, respectively, resulting from applying POD analysis to a horizontal plane at hub height under low-turbulence and ABL flow.

Considering the low-turbulence inflow conditions, Fig. 18a shows an energy distribution across modes that closely resembles that of the vertical plane (displayed in Fig. 10c), with a clear mode pairing situation between modes 1 and 2, followed by three modes with similar energy content. When looking at the spatial modes displayed in Fig. 19a, the results show two mode pairing situations (modes 1-2 and modes 4-5), along with two other modes related to side-to-side meandering (modes 3-6). This is the exact same behaviour as the one presented by the spatial modes on a vertical plane in Fig. 11c. Finally, a similar

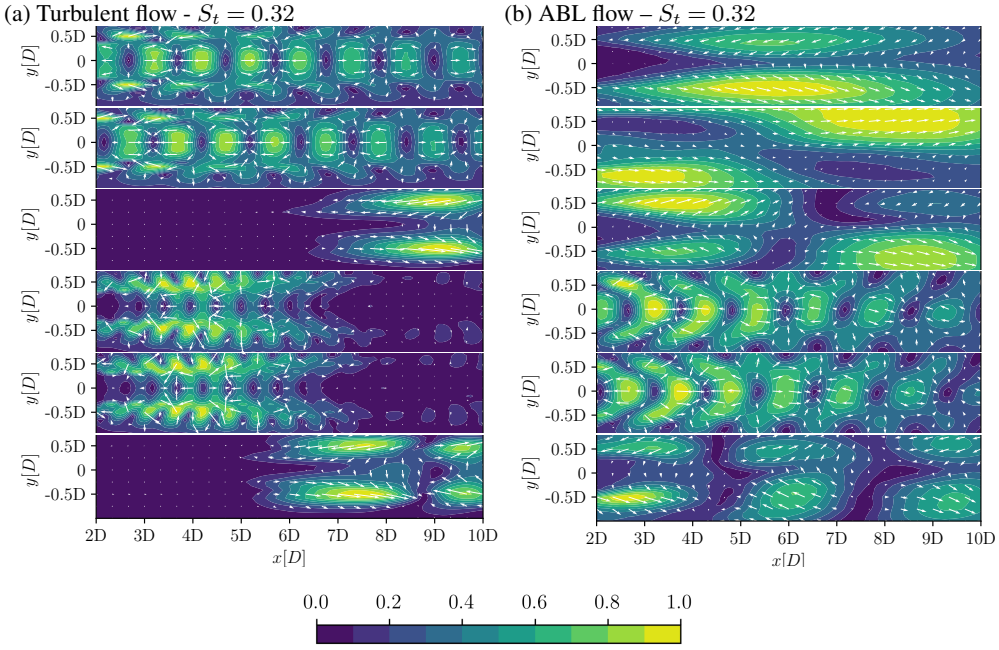

Figure 19. First 6 spatial modes $\Phi_1(\mathbf{x}) - \Phi_6(\mathbf{x})$ resulting from POD analysis applied to a horizontal plane on cases with $S_t = 0.32$ under low-turbulence flow (a) and ABL flow (b).

situation happens when comparing the Fourier spectra of the temporal modes for vertical and horizontal planes (not shown here). These observations allow to conclude that under low-turbulence inflow conditions, the meandering is present in both vertical and horizontal directions. Given the averaged uniformity of the inflow, it is expected that meandering will occur in the same manner in all directions, as there are no preferred directions.

In contrast, a distinct scenario emerges when considering a horizontal plane for the ABL inflow conditions. Firstly, the energy content of the modes is displayed in Fig. 18b. In this figure, a mode pairing situation can be distinguished between modes 4 and 5, as opposed to the modes 2 and 3, as was the case for the vertical plane (Figs. 14c and 15c). In addition, the first mode exhibits a significantly higher energy level in comparison to the subsequent modes, a phenomenon that bears a notable resemblance to the observations presented in Fig. 14c. However, the remaining modes demonstrate a divergent energy content pattern. A detailed analysis of the spatial modes depicted in Fig. 19b reveals significant disparities when compared to the vertical plane modes illustrated in Fig. 15c. The two most energetic modes, which in the previous case were related to the inlet flow, show a different pattern in terms of the spatial modes. Upon analysis of the Fourier spectra in Fig. 20a, it is evident that both modes exhibit a comparable frequency range to the initial two modes observed in the vertical plane case (illustrated in Fig. 16a). This observation suggests that the underlying cause may be the same in both cases. In addition, spatial modes 4 and 5, which are associated with the vortex ring structure, demonstrate a symmetrical pattern with regard to velocity direction until 7D downstream, as illustrated by the arrows. Beyond this point, the mode begins to manifest signs of asymmetry. This finding suggests that, in a significant proportion of the wake, the vortex ring structure does not exhibit lateral meandering, in

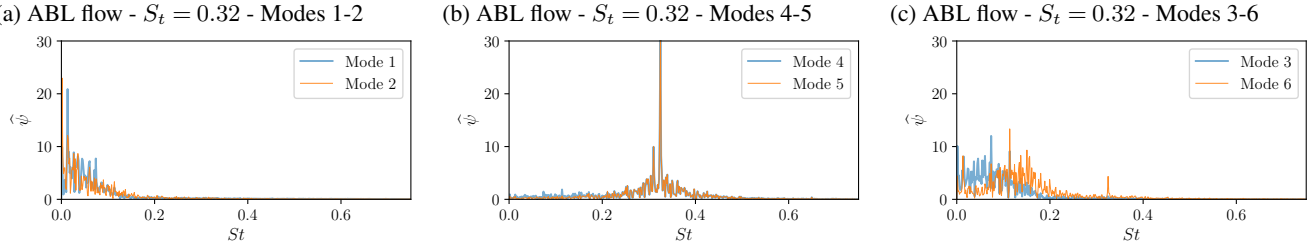

Figure 20. Fourier spectrum of the temporal modes $\Psi_1(t)$ and $\Psi_2(t)$ (a), $\Psi_4(t)$ and $\Psi_5(t)$ (b) and $\Psi_3(t)$ and $\Psi_6(t)$ (c) for $S_t = 0.32$ under ABL flow.

contrast to the vertical meandering observed in modes 2 and 3 of Fig. 15c. As demonstrated in Fig. 20b, the Fourier spectra of both modes indicate the absence of any external signal, confirming the presence of a signal exclusively belonging to this structure. In this instance, the modes appear to be more analogous to those observed in the low-turbulence flow case.

Finally, spatial modes 3 and 6 demonstrate a complex pattern that can initially be difficult to identify. At an initial stage, spatial modes 2 and 3 appear analogous; however, a discrepancy in their frequencies prevents a valid basis for the grouping of mode 3 with the inlet flow. A thorough examination of the spatial mode depicted in Fig. 19b reveals that, in the initial phase, the mode undergoes a clockwise rotation during the first half of the wake, followed by a counter-clockwise rotation in the subsequent phase. As is evident in Mode 6, a similar behaviour is exhibited, yet it is divided into three distinct sections. It can thus be theorised that both modes are related to side-to-side meandering. As demonstrated in Fig. 20c, an analysis of the frequency spectra indicates that both modes exhibit a range of frequencies below $S_t = 0.2$. However, the second mode demonstrates a higher frequency range than the first, due to presenting smaller structures in the spatial mode. Furthermore, in mode 6, a minor peak can be observed at the surge frequency, indicating a minimal presence of surge motion within the mode. However, in contrast to the vertical behaviour, the overall lateral meandering remains physically decoupled from the dynamics of the surge-induced vortex rings.~~the overall lateral meandering exhibited does not appear to be associated with the surge motion, in contrast to the vertical meandering.~~[rev]

5 Phase Average

The pairing modes visible in Figs. 8, 11 and 15 reveal that the intensity of velocity fluctuations varies depending on the downwind distance, reaching a maximum at a point that depends on each case. The next stage of the analysis focuses on this spatial variation. For this purpose, a phase averaging procedure is applied to the data planes where the local mean~~corresponding local average~~[rev] velocity is subtracted~~substracted~~[rev] in each point. First, the planes of data are re-sampled by linear interpolation to obtain exactly 25 planes within the surge period of each case. Then, every plane is averaged with those sharing the same phase, resulting in 25 planes that contain the averaged fluctuations of one complete surge cycle, $\widetilde{u}'(\mathbf{x}, t)$. Only the fluctuation of the streamwise velocity component was considered in this analysis. Figure 21 shows five planes evenly distributed over the

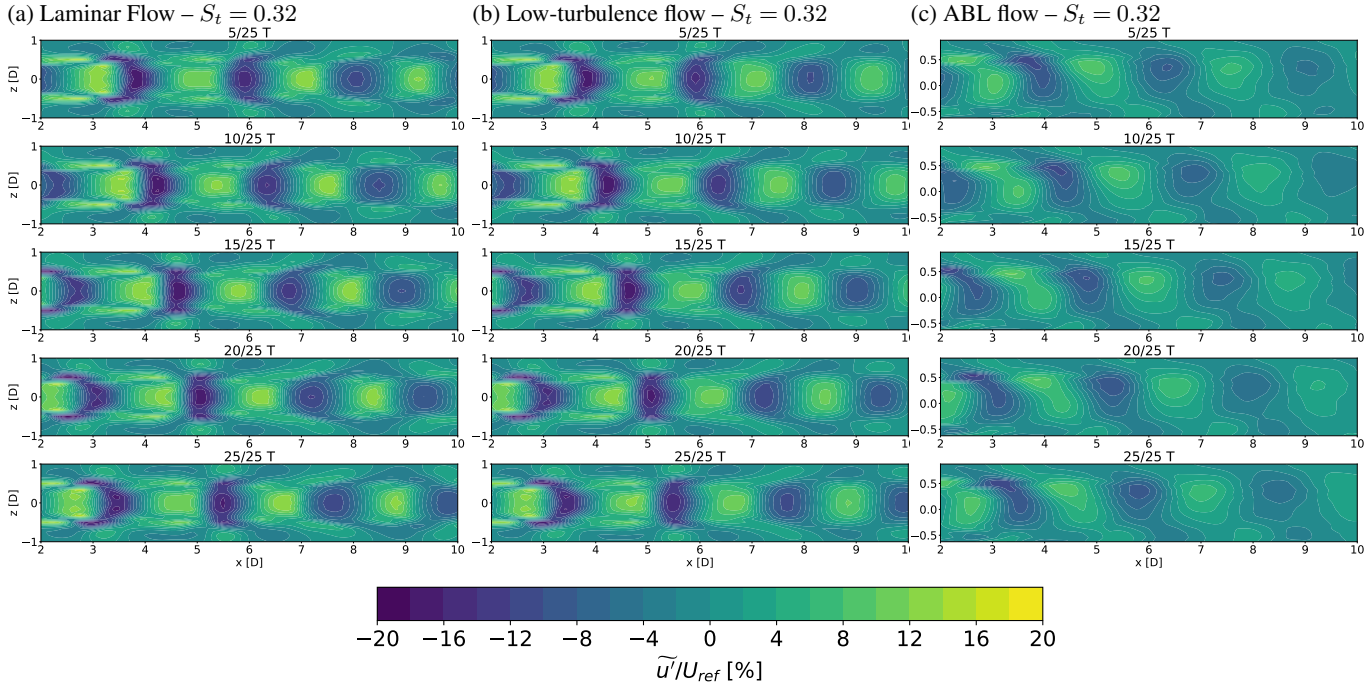

Figure 21. Phase averaged streamwise velocity fluctuations for laminar flow (a), low-turbulence flow (b) and ABL flow (c). Out of the 25 averaged planes within the surge period, 5 planes uniformly distributed are shown.

surge period for $S_t = 0.32$ in the laminar, low-turbulence and ABL flow cases. The results are presented as a percentage of U_{ref}.

The propagation of the structure associated with the surge frequency is visible in all three cases. While the overall configuration remains largely similar, a slight diffusion in the intensity of the velocity oscillations can be observed for the low-turbulence case compared to laminar conditions~~A negligible discrepancy in the configuration of the structure is discernible when contrasting low-turbulence and laminar conditions~~[rev] (Figs. 21a and 21b respectively). As demonstrated in section 4, the shapes are found to be symmetrical with respect to the AD centreline. It is worth noting that the structural patterns in the phase-averaged fields appear at half the frequency of those in the POD modes, since the phase average preserves the velocity sign whereas the POD representation in section 4 reflects the velocity magnitude.[rev] Conversely, for the ABL case (Fig. 21c) the configuration of the structure is modified by the ABL's shear flow. Moreover, the ABL case presents the maximal velocity variations at approximately one quarter of the diameter above the centre of the disk. In contrast, in the other cases, these values appear at the centre of the disk. This result aligns closely with the findings reported in Schliffke et al. (2024), where the highest signature values were observed in the wake at points situated along a vertical line positioned above the disk centre. Regarding the structural patterns, in both the laminar and low-turbulence cases, the regions of minimum fluctuation along the AD centreline appear to merge with off-centre zones, forming an upstream-facing curvature (towards the left) in the near wake ($x < 5D$). Further downstream, this pattern seems to invert into downstream-facing arcs. This behaviour could be attributed to

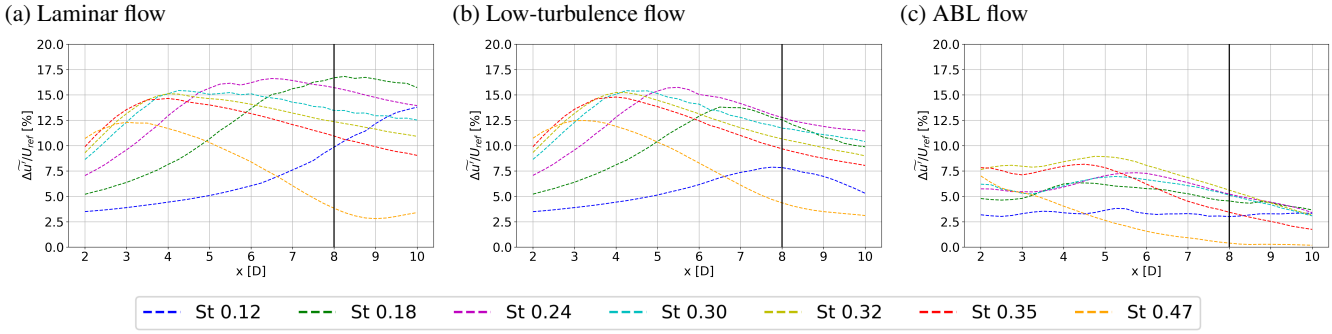

Figure 22. Half amplitude between the maximum and minimum value for the phase-averaged velocity fluctuation within one period. Laminar and low-turbulence values are extracted at the AD centre, while ABL values are extracted at $\frac{D}{4}$ above the AD centre.

the difference in advection velocities inside and outside the wake, a hypothesis that will be thoroughly analysed in the subsequent subsection. In the ABL scenario, the lower-fluctuation structures initially exhibit a downstream tilt up to $x \approx 4D$, likely resulting from the reduced advection velocity below the centreline caused by the shear flow. Beyond this point, an apparent sudden shift in inclination occurs, which may be caused by the merging of a low-velocity region from one structure with the subsequent one. Given the complexity of these flow features, they will be examined in greater detail and with clearer visualisations in the following subsection.~~In addition, the ABL structures appear to be inclined to the left, which could result in a gradual, height-dependent impact on downstream turbines. This tendency undergoes a discernible shift to the centre as the flow deviates from the AD position. A more thorough investigation of this feature will be conducted in the subsequent section.~~[rev]

Sampling along a line at the vertical position where the maximum oscillation occurs (the centre ($z = 0$) for laminar and low-turbulence flows and $z = \frac{1}{4}D$ for ABL) and recording half the amplitude between the maximum and minimum values reveals the spatial propagation dynamics of the pulsating mode, as shown in Fig. 22. The majority of cases demonstrate an initial increase, subsequently followed by a decline in amplitude throughout the wake. In the laminar case (Fig. 22a), as the frequency increases, the amplitude peak is presented closer to the AD and the decay begins sooner in the wake. In particular, the case of $S_t = 0.47$ shows the fastest decay. Also, lower frequencies exhibit higher amplitude peaks, with the exception of $S_t = 0.12$. It is possible that a higher peak may be present further in the wake for this case, although this point is not attained in the present study. Considering a reference distance of 8D from the AD, which was described as an optimum balance for large offshore wind farms by Sørensen et al. (2021), it can be observed that, with the exception of the highest frequency, all cases present a fluctuation of over 10% and even over 15% of the inlet velocity.

In the case of low-turbulence flow (Fig. 22b), all cases show a faster decay of the signal towards the end, with the exception of the highest frequency, which shows a similar behaviour than in the laminar case, with the peak value at 3D and a continuous decay until 9D[rev]. In particular, when comparing with the laminar inflow,[rev] the most affected cases seem to be the lower frequencies, $S_t = 0.12 - 0.24$, as their shift towards the AD, producing an earlier onset of decay compared to previous observations. As demonstrated in section 4, the aforementioned cases exhibited the lowest energy levels in the vortex ring structure. Contrary to this, the cases with higher energy content in section 4, $S_t = 0.30 - 0.35$ exhibit a peak close to 4D, both with and

without turbulence. This may indicate that for those frequencies that favour the energy content of the vortex ring structure, the growth rate and spatial propagation up to the peak value is unaffected by turbulence. Finally, for the highest frequency, $S_t = 0.47$, the spatial behaviour remains almost unaltered, although the decay was already rapid under laminar flow. It is notable that all cases maintain an amplitude almost over 10% at 8D from the AD, with the exception of the highest and lowest frequencies.

Finally, in the ABL flow case (Fig. 22c), it is evident that all cases display a more pronounced decay towards the end than in previous inflow conditions. Nonetheless, the case $S_t = 0.32$, which demonstrated the higher energy content in section 4, exhibits a higher amplitude throughout the entire wake. In addition, the case for $S_t = 0.12$ that previously exhibited no mode pairing related to the vortex ring structure, maintains a low amplitude for the entire wake, demonstrating an absence of ascending-descending behaviour. Once again, $S_t = 0.47$ exhibits accelerated decay. It can be pointed out then that, similar to the low-turbulence case, the spatio-temporal behaviour of the structure deviates from the ideal laminar inflow conditions, and the extent of deviation is contingent on the energy content of the vortex structure for a given surge frequency. This specific behaviour is not observed in the highest frequency case, wherein the decay always exhibits a faster rate. Comparing with the inlet velocity, three of the analysed cases remain with an amplitude over 5% at 8D, while the remaining cases exhibit a decay that falls below this threshold.

A thorough examination of the three plots in Fig. 22 reveals that the strongest surge motion signature in the wake at 8D occurs at $S_t = 0.18$ for laminar flow, $S_t = 0.24$ for low-turbulence flow, and $S_t = 0.32$ for ABL flow. However, it is important to note that this observation should not be confused with the energy content discussed previously in section 4, as the present analysis focuses on the response at a specific height, whereas the earlier analysis considered the vortex structure at all heights.

5.1 Spatio-temporal wake modulation~~Analysis of the inclined structures~~[rev]

As demonstrated in section 4, while the surge motion generates decoupled vortex ring structures under uniform inflows, the ABL shear flow couples with these structures to induce a synchronised vertical meandering. Furthermore, distinct spatial patterns emerge depending on the inflow, ranging from symmetric wake modulation to a noticeable structural inclination of the velocity fluctuations in the atmospheric scenario (as illustrated in Fig. 21c). In this section, a more profound examination of these varied wake configurations is proposed.[rev] To this end, the velocity deficit will be subjected to phase averaging in place of velocity fluctuations. This approach is intended to provide a more precise depiction of the wake's configuration during surge motion. The process is analogous to the previous analysis, but rather than subtracting the mean flow values, the inflow profiles displayed in Figs. 4a and 5a are subtracted considering the corresponding case. Once again, 25 planes are obtained, containing in this instance the velocity deficit, $\widetilde{\Delta u}(\mathbf{x}, t)$. In this analysis, the focus was exclusively on the streamwise velocity component. Figure 23 illustrates one of the frames for $S_t = 0.32$ in the laminar, low-turbulence and ABL flow cases. The results are presented as percentage of U_{ref}.

In the laminar and low-turbulence cases, illustrated in Figs. 23a and 23b, averaged velocity deficit exhibits a wake modulated by an expansion and contraction due to[rev] the surge motion. This behaviour aligns closely with the synchronised *coherent pulsing* experimentally observed by Messmer et al. (2024) under laminar inflow at a comparable Strouhal number ($St = 0.38$

vs. $St = 0.32$). Furthermore, recent atmospheric wind tunnel tests by Hubert et al. (2025) confirmed that these periodic wake expansions persist even at a lower frequency ($St = 0.11$), while numerical evaluations attribute this overall dynamic to strong variations in the rotor's axial induction (Sivalingam et al., 2018). [rev] As demonstrated in the case of fluctuations in Fig. 21, there is a minimal~~negligible~~[rev] difference between laminar and low-turbulence inflow with regard to this aspect. The only discernible discrepancy manifests towards the culmination of the wake, in proximity to 10D, where the contraction is more pronounced in the laminar inflow scenario. Conversely, in the context of ABL flow, as illustrated in Fig. 23c, the phase average deficit reveals a wake characterised by traces of contraction and expansion, coupled with a vertical deformation induced by the background wind shear~~in addition to the vertical meandering previously examined in Fig. 15c~~[rev]. Red lines on the three figures connect the expansion tops and bottoms for the first three cycles in each case. For the first two scenarios, the lines maintain a parallel configuration throughout the wake. It is evident that, in the initial line on the left, the maximum deficit is situated to the right of the red line. For the second and third lines, the maximum deficit is observed to the left of the line. This phenomenon is attributable to a disparity in advection velocity, whereby maximum deficit structures travel slower within the wake in comparison to the expansion and contraction observed at the periphery of the wake. The lines in the ABL case, in contrast to the first two cases, show an inclination towards the right. Furthermore, it has an increasing tendency the further away from the AD original position. This phenomenon is attributable to the effects of shear flow, which modify the translation velocity of the vortex structure above and below the AD centreline. As was evidenced in preceding cases, the expansion regions situated above the wake appear to travel faster than the maximum deficit structures. However, it is now evident that the expansion regions situated below the wake travel slower. Consequently, this disparity in translation velocities causes the surge motion to couple with the shear flow, inducing a synchronised vertical meandering. This phenomenon was also observed by Hubert et al. (2026), who conducted a SPIV analysis at 8.125D from the position of a porous disk under surge motion.[rev] In addition, the configuration of the maximum deficit structures appears to undergo a transformation throughout the wake, as evidenced by the iso-deficit lines. ~~Consequently, the meandering phenomenon is triggered when surge motion is combined with shear flow.~~ [rev] Furthermore, an increase in velocity above the AD centreline results in a greater force acting on the top than on the bottom, leading to greater fluctuations over the AD axis. ~~This phenomenon is elucidated by the observation of an inclination to the left in Fig. 21c, which undergoes a rightward shift in the further distance from the AD original position, attributable to different translation velocities.~~[rev]

6 Conclusions

In this work, new physical insights were achieved regarding the vortex ring structure that appears downstream of a FOWT model under surge motion, by comparing its dynamics under realistic ABL conditions against laminar and low-turbulence flows.~~In this work, a new level of analysis was achieved regarding the vortex ring structure that appears downstream of a FOWT model under surge motion.~~[rev] The structure was first visualised by means of the Q-criterion for laminar and low-turbulence uniform inflows, while no discernible pattern was observed under ABL inflow, in line with previous works. Subsequently, a POD analysis was conducted for the three inflow conditions. In the laminar flow configuration, the method allocated more

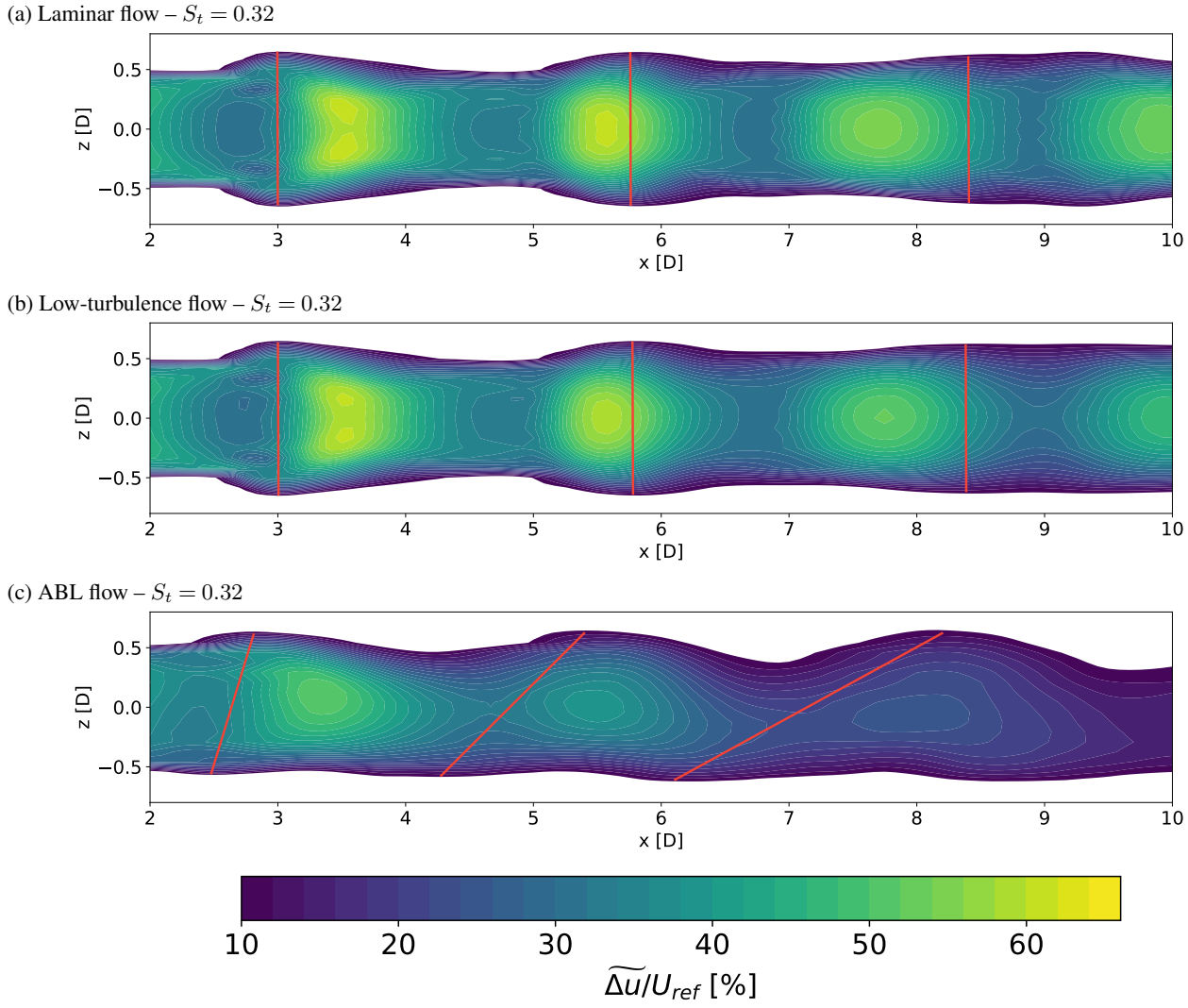

Figure 23. Phase averaged streamwise velocity deficit for laminar flow (a), low-turbulence flow (b) and ABL flow (c). For each case, only 1 out of the 25 averaged planes is shown. Red lines connect the expansion tops and bottoms for the first three cycles in each case.

than 99% of the energy to the vortex ring structure generated by the harmonic surge motion applied to the actuator disk, displaying pairs of opposite modes associated with the surge frequency and multiple harmonics. In this instance, all modes displayed symmetry with respect to the AD centreline, indicating no meandering phenomenon. Additionally, the low-turbulence case also displayed pairs of opposite modes related to the vortex ring structure which were symmetric in terms of velocity direction. Yet, these were combined with non-symmetric modes related to the no-motion case, which were linked to wake meandering phenomenon. The energy content analysis confirmed that the signature related to the vortex ring structure shows a local maximum in the studied frequency range.

In the context of the ABL inflow scenario, a divergent tendency was identified, manifesting a single pair of opposite modes associated with the surge frequency and two high-energy modes linked to the inlet flow. The latter were observed in both motion and no-motion cases. In this instance, no harmonic of the surge frequency was excited within the most energetic modes. Furthermore, in cases involving a moving AD, the modes related to the vortex ring structure exhibited asymmetry with respect to the AD centreline, thereby indicating the presence of meandering in such modes. In the absence of any other significant peaks in the Fourier spectra, it can be concluded that under ABL conditions, the combination of surge kinematics and background shear couples to induce a synchronised vertical meandering. A more thorough investigation into the meandering phenomenon revealed that, while meandering occurs in every direction with equal intensity for the low-turbulence inflow case, under ABL conditions the lateral and vertical meandering are produced by different factors. While the vertical meandering is strongly linked to the surge motion, the lateral meandering remains physically decoupled from the vortex ring dynamics and is driven by different atmospheric factors.[rev] In both low-turbulence and ABL inflows, the highest energy content structures manifested at S_t values consistent with those observed in previous experiments. However, distinct behaviours were observed, with the ABL case exhibiting a narrower energy distribution. It was determined that the no-motion modes were more significant under ABL than under low-turbulence inflow. Consequently, the generation of structures related to the vortex ring structure with higher energy was observed in the latter.

The phase-averaged analysis on velocity fluctuations yielded further insights into the spatio-temporal dynamics, propagation and growth rates of the structure, and how these are affected by inlet conditions. In laminar and low-turbulence cases the structure demonstrated a symmetrical configuration. However, in the ABL case, the shear flow modified the modes thereby shifting the location of fluctuation extrema, which is consistent with previous experimental observations. Furthermore, both low-turbulence and ABL flow showed a diminished impact on growth rate for those frequencies that developed the most energetic structures. In both cases, the decay towards the end was faster than under laminar inflow. Finally, the majority of cases exhibited an amplitude in over 10% of the inlet velocity at 8D downstream from the AD, under low-turbulence flow, which aligns closely with the findings observed in laminar inflow conditions. In contrast, for the ABL case, this value declined to approximately 5% or less, depending on the specific case scenario.

Finally, to obtain a thorough analysis on the shape of the wake, phase-average was applied to the velocity deficit. The present study has demonstrated that, in laminar and low-turbulence cases, the wake is modulated by an expansion and contraction in response to surge motion. This periodic behaviour firmly corroborates the phase-locked coherent pulsing documented in recent wind tunnel experiments at comparable Strouhal numbers. ~~as was evidenced in previous experiments~~[rev]. Conversely, under

ABL flow, the study revealed traces of this modulation coupled with a vertical deformation induced by the background wind shear.~~combined with vertical meandering~~[rev]. This phenomenon was attributed to the disparity in translation velocity between the lower and upper regions of the structure. This phenomenon was also visualised in recent wind tunnel experiments under ABL conditions.

Despite the robustness of the AD model in capturing the far-wake evolution, this approach inherently bypasses the initial generation of discrete helical tip vortices and their subsequent breakdown into vortex ring structures. Consequently, future work should extend this analysis using ALM or blade-resolved simulations to capture these near-wake dynamics and investigate how these helical tip vortices behave and transition under realistic ABL conditions.[rev] Overall, this study establishes that while the surge-induced wake modulation and its energy-frequency dependence persist across different inflows, the highly turbulent and sheared nature of the ABL introduces unique dynamics. Specifically, the combined effects of atmospheric shear and elevated background turbulence not only structurally deform the wake but also induce a directional decoupling of the meandering phenomenon.~~Overall, the study highlighted that the vortex ring structure exhibits a significantly different behaviour depending on the inflow conditions. In particular, the presence of ABL shear not only modifies the spatial shape of the modes but also strongly influences their amplification and energy distribution.~~[rev] These findings emphasize the need for further research under realistic atmospheric conditions, where Marine Atmospheric Boundary Layer thermal stability should be taken into account in the analysis of FOWT wakes.

Code availability

The SOWFA CFD tool is made available by NREL (https://github.com/NREL/SOWFA/; NREL, 2024).

Author contributions

DAB, ADO and SA were responsible for conceptualization and methodology during this research. DAB performed the numerical simulations. SA was responsible for providing the experimental results. The original draft was written by DAB and reviewed and edited by ADO, RS and SA.

Competing interests

One of the co-authors is a member of the editorial board of the journal Wind Energy Science.

Acknowledgements

This work used computational resources from UNC Supercómputo (CCAD), which is part of SNCAD, Argentina. Also, the authors would like to acknowledge the computational time in the TUPAC cluster, made available by the CSC-CONICET, and École Centrale Nantes for providing the experimental measurements.

Financial support

The authors would like to acknowledge the University of Buenos Aires for the funds received through grant 20620190100001BA. Furthermore, DAB would like to express his gratitude to the 2023 UBAINT Doctoral Program of UBA for the financial support.

References

Ali, N., Calaf, M., and Cal, R. B.: Cluster-based probabilistic structure dynamical model of wind turbine wake, Journal of Turbulence, 22, 497–516, 2021.

Allen, C., Viscelli, A., Dagher, H., Goupee, A., Gaertner, E., Abbas, N., Hall, M., and Barter, G.: Definition of the UMaine VolturnUS-S reference platform developed for the IEA wind 15-megawatt offshore reference wind turbine, Tech. rep., National Renewable Energy Laboratory (NREL), 2020.

Andersen, S. J., Sørensen, J. N., and Mikkelsen, R.: Reduced order model of the inherent turbulence of wind turbine wakes inside an infinitely long row of turbines, Journal of Physics: Conference Series, 555, 012 005, https://doi.org/10.1088/1742-6596/555/1/012005, 2014.

Arabgolarcheh, A., Micallef, D., Rezaeiha, A., and Benini, E.: Modelling of two tandem floating offshore wind turbines using an actuator line model, Renewable Energy, 216, 119 067, 2023a.

Arabgolarcheh, A., Rouhollahi, A., and Benini, E.: Analysis of middle-to-far wake behind floating offshore wind turbines in the presence of multiple platform motions, Renewable Energy, 208, 546–560, 2023b.

Aubrun, S., Bastankhah, M., Cal, R., Conan, B., Hearst, R., Hoek, D., Hölling, M., Huang, M., Hur, C., Karlsen, B., Neunaber, I., Obligado, M., Peinke, J., Percin, M., Saetran, L., Schito, P., Schliffke, B., Sims-Williams, D., Uzol, O., Vinnes, M., and Zasso, A.: Round-robin tests of porous disc models, Journal of Physics: Conference Series, 1256, 012 004, https://doi.org/10.1088/1742-6596/1256/1/012004, 2019.

Bak, C., Zahle, F., Bitsche, R., Kim, T., Yde, A., Henriksen, L. C., Hansen, M. H., Blasques, J. P. A. A., Gaunaa, M., and Natarajan, A.: The DTU 10-MW reference wind turbine, in: Danish wind power research 2013, 2013.

Barile, D. A., Sosa, R., Aubrun, S., and Otero, A. D.: Wake study of a FOWT model under surge motion: a POD analysis, in: Wind Energy Science Conference, European Academy of Wind Energy; Centrale Nantes, June 2025, Nantes, France., 2025.

Bastine, D., Witha, B., Wächter, M., and Peinke, J.: POD Analysis of a Wind Turbine Wake in a Turbulent Atmospheric Boundary Layer, Journal of Physics: Conference Series, 524, 012 153, https://doi.org/10.1088/1742-6596/524/1/012153, 2014.

Bastine, D., Witha, B., Wächter, M., and Peinke, J.: Towards a Simplified DynamicWake Model Using POD Analysis, Energies, 8, 895–920, https://doi.org/10.3390/en8020895, 2015.

Belvasi, N., Conan, B., Schliffke, B., Perret, L., Desmond, C., Murphy, J., and Aubrun, S.: Far-Wake Meandering of a Wind Turbine Model with Imposed Motions: An Experimental S-PIV Analysis, Energies, 15, https://doi.org/10.3390/en15207757, 2022.

Chen, Z., Wei, C., Chen, Z., Wang, S., and Tang, L.: Numerical Simulation of Atmospheric Boundary Layer Turbulence in a Wind Tunnel Based on a Hybrid Method, Atmosphere, 13, https://www.mdpi.com/2073-4433/13/12/2044, 2022.

Cherubini, S., Cillis, G. D., Semeraro, O., Leonardi, S., and Palma, P.: How incoming turbulence affects wake recovery of an NREL-5MW wind turbine, Journal of Physics: Conference Series, 2385, 012 139, https://doi.org/10.1088/1742-6596/2385/1/012139, 2022.

Churchfield, M., Lee, S., Moriarty, P., Martinez, L., Leonardi, S., Vijayakumar, G., and Brasseur, J.: A large-eddy simulation of wind-plant aerodynamics, in: 50th AIAA aerospace sciences meeting including the new horizons forum and aerospace exposition, p. 537, 2012a.

Churchfield, M. J., Lee, S., Michalakes, J., and Moriarty, P. J.: A numerical study of the effects of atmospheric and wake turbulence on wind turbine dynamics, Journal of turbulence, p. N14, 2012b.

Duan, L., Sun, Q., He, Z., and Li, G.: Wake topology and energy recovery in floating horizontal-axis wind turbines with harmonic surge motion, Energy, 260, 124 907, 2022.

Farrugia, R., Sant, T., and Micallef, D.: A study on the aerodynamics of a floating wind turbine rotor, Renewable energy, 86, 770–784, 2016.

Fontanella, A., Bayati, I., Mikkelsen, R., Belloli, M., and Zasso, A.: UNAFLOW: a holistic wind tunnel experiment about the aerodynamic response of floating wind turbines under imposed surge motion, Wind Energy Science, 6, 1169–1190, https://doi.org/10.5194/wes-6-1169-2021, 2021.

Fontanella, A., Facchinetti, A., Di Carlo, S., and Belloli, M.: Wind tunnel investigation of the aerodynamic response of two 15 MW floating wind turbines, Wind Energy Science, 7, 1711–1729, https://doi.org/10.5194/wes-7-1711-2022, 2022a.

Fontanella, A., Zasso, A., and Belloli, M.: Wind tunnel investigation of the wake-flow response for a floating turbine subjected to surge motion, Journal of Physics: Conference Series, 2265, 042 023, https://doi.org/10.1088/1742-6596/2265/4/042023, 2022b.

Gaertner, E., Rinker, J., Sethuraman, L., Zahle, F., Anderson, B., Barter, G., Abbas, N., Meng, F., Bortolotti, P., Skrzypinski, W., et al.: Definition of the IEA 15-megawatt offshore reference wind turbine, 2020.

Hamilton, N., Viggiano, B., Calaf, M., Tutkun, M., and Cal, R. B.: A generalized framework for reduced-order modeling of a wind turbine wake, Wind Energy, 21, 373–390, https://doi.org/https://doi.org/10.1002/we.2167, 2018.

Hodgson, E. L., Andersen, S. J., Troldborg, N., Forsting, A. M., Mikkelsen, R. F., and Sørensen, J. N.: A Quantitative Comparison of Aeroelastic Computations using Flex5 and Actuator Methods in LES, Journal of Physics: Conference Series, 1934, 012 014, https://doi.org/10.1088/1742-6596/1934/1/012014, 2021.

Hubert, A., Conan, B., and Aubrun, S.: Spatiotemporal behavior of the far wake of a wind turbine model subjected to harmonic motions: phase averaging applied to stereo particle image velocimetry measurements, Wind Energy Science, 10, 1351–1368, https://doi.org/10.5194/wes-10-1351-2025, 2025.

Hubert, A., Conan, B., and Aubrun, S.: Experimental investigation of harmonic surge motions on the far wake of a wind turbine model and analysis of a resulting sub-harmonic wake response, to be submitted to Wind Energy Science, XX, XX, https://doi.org/XX, 2026.

Immer, M. C.: Time-resolved measurement and simulation of local scale turbulent urban flow, Ph.D. thesis, ETH Zurich, 2016.

Iungo, G. V., Santoni-Ortiz, C., Abkar, M., Porté-Agel, F., Rotea, M. A., and Leonardi, S.: Data-driven Reduced Order Model for prediction of wind turbine wakes, Journal of Physics: Conference Series, 625, 012 009, https://doi.org/10.1088/1742-6596/625/1/012009, 2015.

Jimenez, A., Crespo, A., Migoya, E., and Garcia, J.: Advances in large-eddy simulation of a wind turbine wake, Journal of Physics: Conference Series, 75, 012 041, https://doi.org/10.1088/1742-6596/75/1/012041, 2007.

Johlas, H. M., Martínez-Tossas, L. A., Schmidt, D. P., Lackner, M. A., and Churchfield, M. J.: Large eddy simulations of floating offshore wind turbine wakes with coupled platform motion, Journal of Physics: Conference Series, 1256, 012 018, https://doi.org/10.1088/1742-6596/1256/1/012018, 2019.

Johlas, H. M., Martínez-Tossas, L. A., Lackner, M. A., Schmidt, D. P., and Churchfield, M. J.: Large eddy simulations of offshore wind turbine wakes for two floating platform types, Journal of Physics: Conference Series, 1452, 012 034, https://doi.org/10.1088/1742-6596/1452/1/012034, 2020.

Klein, M., Sadiki, A., and Janicka, J.: A digital filter based generation of inflow data for spatially developing direct numerical or large eddy simulations, Journal of Computational Physics, 186, 652–665, https://doi.org/https://doi.org/10.1016/S0021-9991(03)00090-1, 2003.

Kleine, V. G., Franceschini, L., Carmo, B. S., Hanifi, A., and Henningson, D. S.: The stability of wakes of floating wind turbines, Physics of Fluids, 34, 2022.

Kopperstad, K. M., Kumar, R., and Shoele, K.: Aerodynamic characterization of barge and spar type floating offshore wind turbines at different sea states, Wind Energy, 23, 2087–2112, 2020.

Lanzilao, L. and Meyers, J.: An improved fringe-region technique for the representation of gravity waves in large eddy simulation with application to wind farms, Boundary-layer meteorology, 186, 567–593, 2023.

Lee, H. and Lee, D.-J.: Effects of platform motions on aerodynamic performance and unsteady wake evolution of a floating offshore wind turbine, Renewable Energy, 143, 9–23, https://doi.org/https://doi.org/10.1016/j.renene.2019.04.134, 2019.

Lumley, J. L.: The structure of inhomogeneous turbulent flows, Atmospheric turbulence and radio wave propagation, pp. 166–178, 1967.

Messmer, T., Hölling, M., and Peinke, J.: Enhanced recovery caused by nonlinear dynamics in the wake of a floating offshore wind turbine, Journal of Fluid Mechanics, 984, A66, https://doi.org/10.1017/jfm.2024.175, 2024.

Mikkelsen, R.: Actuator Disc Methods Applied to Wind Turbines, Ph.D. thesis, ISBN 87-7475-296-0, 2004.

Navarro Diaz, G. P., Saulo, A. C., and Otero, A. D.: Comparative study on the wake description using actuator disc model with increasing level of complexity, Journal of Physics: Conference Series, 1256, 012 017, https://doi.org/10.1088/1742-6596/1256/1/012017, 2019a.

Navarro Diaz, G. P., Saulo, A. C., and Otero, A. D.: Wind farm interference and terrain interaction simulation by means of an adaptive actuator disc, Journal of Wind Engineering and Industrial Aerodynamics, 186, 58–67, https://doi.org/https://doi.org/10.1016/j.jweia.2018.12.018, 2019b.

Navarro Diaz, G. P., Saulo, A. C., and Otero, A. D.: Full wind rose wind farm simulation including wake and terrain effects for energy yield assessment, Energy, 237, 121 642, https://doi.org/https://doi.org/10.1016/j.energy.2021.121642, 2021.

Navarro Diaz, G. P., Otero, A. D., Asmuth, H., Sørensen, J. N., and Ivanell, S.: Actuator line model using simplified force calculation methods, Wind Energy Science, 8, 363–382, https://doi.org/10.5194/wes-8-363-2023, 2023.

Ninni, D. and Mendez, M. A.: MODULO: A software for Multiscale Proper Orthogonal Decomposition of data, SoftwareX, 12, 100 622, https://doi.org/https://doi.org/10.1016/j.softx.2020.100622, 2020.

NREL: SOWFA: Simulator fOr Wind Farm Applications, https://github.com/NatLabRockies/SOWFA, accessed: 2026-04-09, 2012.

Nybø, A., Gunnar Nielsen, F., and Godvik, M.: Sensitivity of the dynamic response of a multimegawatt floating wind turbine to the choice of turbulence model, Wind Energy, 25, 1013–1029, https://doi.org/https://doi.org/10.1002/we.2712, 2022.

OpenCFD-Ltd: OpenFOAM, https://www.openfoam.com/, accessed: 2024-12-10, 2004.

Porté-Agel, F., Wu, Y.-T., Lu, H., and Conzemius, R. J.: Large-eddy simulation of atmospheric boundary layer flow through wind turbines and wind farms, Journal of Wind Engineering and Industrial Aerodynamics, 99, 154–168, https://doi.org/https://doi.org/10.1016/j.jweia.2011.01.011, the Fifth International Symposium on Computational Wind Engineering, 2011.

Raibaudo, C., Piquet, T., Schliffke, B., Conan, B., and Perret, L.: POD analysis of the wake dynamics of an offshore floating wind turbine model, Journal of Physics: Conference Series, 2265, 022 085, https://doi.org/10.1088/1742-6596/2265/2/022085, 2022.

Rezaeiha, A. and Micallef, D.: Wake interactions of two tandem floating offshore wind turbines: CFD analysis using actuator disc model, Renewable Energy, 179, 859–876, 2021.

Richards, P. and Hoxey, R.: Appropriate boundary conditions for computational wind engineering models using the k-ε turbulence model, Journal of Wind Engineering and Industrial Aerodynamics, 46-47, 145–153, https://doi.org/https://doi.org/10.1016/0167-6105(93)90124-7, proceedings of the 1st International on Computational Wind Engineering, 1993.

Sarlak, H., Nishino, T., Martínez-Tossas, L., Meneveau, C., and Sørensen, J.: Assessment of blockage effects on the wake characteristics and power of wind turbines, Renewable Energy, 93, 340–352, https://doi.org/https://doi.org/10.1016/j.renene.2016.01.101, 2016.

Schliffke, B., Aubrun, S., and Conan, B.: Wind Tunnel Study of a "Floating" Wind Turbine's Wake in an Atmospheric Boundary Layer with Imposed Characteristic Surge Motion, Journal of Physics: Conference Series, 1618, 062 015, https://doi.org/10.1088/1742-6596/1618/6/062015, 2020.

Schliffke, B., Conan, B., and Aubrun, S.: Floating wind turbine motion signature in the far-wake spectral content – a wind tunnel experiment, Wind Energy Science, 9, 519–532, https://doi.org/10.5194/wes-9-519-2024, 2024.

Schulz, C. W., Netzband, S., Özinan, U., Cheng, P. W., and Abdel-Maksoud, M.: Wind turbine rotors in surge motion: new insights into unsteady aerodynamics of floating offshore wind turbines (FOWTs) from experiments and simulations, Wind Energy Science, 9, 665–695, https://doi.org/10.5194/wes-9-665-2024, 2024.

Schumann, U.: Subgrid scale model for finite difference simulations of turbulent flows in plane channels and annuli, Journal of computational physics, 18, 376–404, 1975.

Sirovich, L.: Turbulence and the dynamics of coherent structures. I. Coherent structures, Quarterly of applied mathematics, 45, 561–571, 1987.

Sivalingam, K., Martin, S., and Singapore Wala, A. A.: Numerical Validation of Floating Offshore Wind Turbine Scaled Rotors for Surge Motion, Energies, 11, https://doi.org/10.3390/en11102578, 2018.

Stevens, R. J., Graham, J., and Meneveau, C.: A concurrent precursor inflow method for large eddy simulations and applications to finite length wind farms, Renewable energy, 68, 46–50, 2014.

Stull, R. B.: An introduction to boundary layer meteorology, vol. 13, Springer Science & Business Media, 2012.

Sørensen, J. N., Larsen, G. C., and Cazin-Bourguignon, A.: Production and Cost Assessment of Offshore Wind Power in the North Sea, Journal of Physics: Conference Series, 1934, 012 019, https://doi.org/10.1088/1742-6596/1934/1/012019, 2021.

Tran, T. and Kim, D.-H.: A CFD study into the influence of unsteady aerodynamic interference on wind turbine surge motion, Renewable Energy, 90, 204–228, https://doi.org/10.1016/j.renene.2015.12.013, 2016.

van der Laan, M. P., Kelly, M., Floors, R., and Peña, A.: Rossby number similarity of an atmospheric RANS model using limited-length-scale turbulence closures extended to unstable stratification, Wind Energy Science, 5, 355–374, https://doi.org/10.5194/wes-5-355-2020, 2020.

van der Laan, M. P., Baungaard, M., and Kelly, M.: Inflow modeling for wind farm flows in RANS, Journal of Physics: Conference Series, 1934, 012 012, https://doi.org/10.1088/1742-6596/1934/1/012012, 2021.

VDI: VDI guideline 3783/12: Environmental meteorology – Physical modelling of flow and dispersion processes in the atmospheric boundary layer – Application of wind tunnels, Berlin, 2000.

VerHulst, C. and Meneveau, C.: Large eddy simulation study of the kinetic energy entrainment by energetic turbulent flow structures in large wind farms, Physics of Fluids, 26, 025 113, https://doi.org/10.1063/1.4865755, 2014.

Wang, T., Cai, C., Liu, J., Peng, C., Wang, Y., Sun, X., Zhong, X., Zhang, J., and Li, Q.: Wake characteristics and vortex structure evolution of floating offshore wind turbine under surge motion, Energy, 302, 131 788, 2024.

Wang, X., Cai, C., Cai, S.-G., Wang, T., Wang, Z., Song, J., Rong, X., and Li, Q.: A review of aerodynamic and wake characteristics of floating offshore wind turbines, Renewable and Sustainable Energy Reviews, 175, 113 144, https://doi.org/https://doi.org/10.1016/j.rser.2022.113144, 2023.

Wen, B., Tian, X., Dong, X., Peng, Z., and Zhang, W.: Influences of surge motion on the power and thrust characteristics of an offshore floating wind turbine, Energy, 141, 2054–2068, https://doi.org/https://doi.org/10.1016/j.energy.2017.11.090, 2017.

Xu, B., Wang, T., Yuan, Y., and Cao, J.: Unsteady aerodynamic analysis for offshore floating wind turbines under different wind conditions, Philosophical Transactions of the Royal Society A: Mathematical, Physical and Engineering Sciences, 373, 20140 080, 2015.

Xu, S., Xue, Y., Zhao, W., and Wan, D.: A Review of High-Fidelity Computational Fluid Dynamics for Floating Offshore Wind Turbines, Journal of Marine Science and Engineering, 10, https://doi.org/10.3390/jmse10101357, 2022.

Xu, S., Zhuang, T., Zhao, W., and Wan, D.: Numerical investigation of aerodynamic responses and wake characteristics of a floating offshore wind turbine under atmospheric boundary layer inflows, Ocean Engineering, 279, 114 527, https://doi.org/https://doi.org/10.1016/j.oceaneng.2023.114527, 2023.

Xu, S., Yang, X., Zhao, W., and Wan, D.: Numerical analysis of aero-hydrodynamic wake flows of a floating offshore wind turbine subjected to atmospheric turbulence inflows, Ocean Engineering, 300, 117 498, https://doi.org/https://doi.org/10.1016/j.oceaneng.2024.117498, 2024.

Yoshizawa, A.: Statistical theory for compressible turbulent shear flows, with the application to subgrid modeling, The Physics of Fluids, 29, 2152–2164, https://doi.org/10.1063/1.865552, 1986.

Zahn, E. and Bou-Zeid, E.: Correction: Setting Up a Large-Eddy Simulation to Focus on the Atmospheric Surface Layer, Boundary-Layer Meteorology, 190, 19, https://doi.org/10.1007/s10546-024-00865-x, 2024.

Zhou, T., Lan, H., Xu, C., Han, X., and Wu, X.: Wake and performance of floating offshore wind turbines under six degrees of freedom conditions, Physics of Fluids, 37, 015 167, https://doi.org/10.1063/5.0246831, 2025.

Zhou, Y., Xiao, Q., Liu, Y., Incecik, A., Peyrard, C., Wan, D., Pan, G., and Li, S.: Exploring inflow wind condition on floating offshore wind turbine aerodynamic characterisation and platform motion prediction using blade resolved CFD simulation, Renewable Energy, 182, 1060–1079, https://doi.org/https://doi.org/10.1016/j.renene.2021.11.010, 2022.